The Astrophysical Journal, 995:181 (37pp), 2025 December 20
https://doi.org/10.3847/1538-4357/ae08a8

Magnetic Fields in the Bones of the Milky Way

Ian W. Stephens[1,2], Simon Coudé[1,2], Philip C. Myers[2], Catherine Zucker[2], James M. Jackson[3], B.-G. Andersson[4], Rowan Smith[5], Archana Soam[6], Patricio Sanhueza[7], Taylor Hogge[8], Howard A. Smith[2], Giles Novak[9], Sarah Sadavoy[10], Thushara Pillai[11], Zhi-Yun Li[12], Leslie W. Looney[13], Koji Sugitani[14], Andrés E. Guzmán[15], Alyssa Goodman[2], Takayoshi Kusune[16], Miaomiao Zhang[17], Nicole Karnath[2,18], and Jessy Marin[2,19]

[1] Department of Earth, Environment, and Physics, Worcester State University, Worcester, MA 01602, USA; istephens@worcester.edu
[2] Center for Astrophysics | Harvard & Smithsonian, 60 Garden Street, Cambridge, MA 02138, USA
[3] Green Bank Observatory, 155 Observatory Road, Green Bank, WV 24944, USA
[4] McDonald Observatory, University of Texas at Austin, 2515 Speedway Boulevard, Austin, TX 78712, USA
[5] SUPA, School of Physics and Astronomy, University of St Andrews, North Haugh, St Andrews, KY16 9SS, UK
[6] Indian Institute of Astrophysics, II Block, Koramangala, Bengaluru 560034, India
[7] Department of Astronomy, School of Science, The University of Tokyo, 7-3-1 Hongo, Bunkyo, Tokyo 113-0033, Japan
[8] Institute for Astrophysical Research, Boston University, 725 Commonwealth Avenue, Boston, MA 02215, USA
[9] Center for Interdisciplinary Exploration and Research in Astrophysics (CIERA), and Department of Physics & Astronomy, Northwestern University, 2145 Sheridan Road, Evanston, IL 60208, USA
[10] Department of Physics, Engineering and Astronomy, Queen's University, 64 Bader Lane, Kingston, ON, K7L 3N6, Canada
[11] MIT Haystack Observatory, 99 MIllstone Road, Westford, MA 01826, USA
[12] Astronomy Department, University of Virginia, Charlottesville, VA 22904, USA
[13] Department of Astronomy, University of Illinois, 1002 West Green Street, Urbana, IL 61801, USA
[14] Graduate School of Science, Nagoya City University, Mizuho-ku, Nagoya, Aichi 467-8501, Japan
[15] National Astronomical Observatory of Japan, National Institute of Natural Sciences, 2-21-1 Osawa, Mitaka, Tokyo 181-8588, Japan
[16] Graduate School of Science, Nagoya University, Chikusa-ku, Nagoya 464-8602, Japan
[17] Purple Mountain Observatory, and Key Laboratory for Radio Astronomy, Chinese Academy of Sciences, 210008 Nanjing, People's Republic of China
[18] Space Science Institute, 4765 Walnut Street, Ste. B, Boulder, CO 80301, USA
[19] Jodrell Bank Centre for Astrophysics, Department of Physics and Astronomy, University of Manchester, Oxford Road, Manchester, M13 9PL, UK

Received 2025 June 11; revised 2025 September 17; accepted 2025 September 17; published 2025 December 15

Abstract

Stars primarily form in galactic spiral arms within dense, filamentary molecular clouds. The largest and most elongated of these molecular clouds are referred to as "bones," which are massive, velocity-coherent filaments (lengths ∼20 to >100 pc, widths ∼1–2 pc) that run approximately parallel and in close proximity to the Galactic plane. While these bones have been generally well characterized, the importance and structure of their magnetic fields (B-fields) remain largely unconstrained. Through the Stratospheric Observatory for Infrared Astronomy Legacy program FIlaments Extremely Long and Dark: a Magnetic Polarization Survey (FIELDMAPS), we mapped the B-fields of 10 bones in the Milky Way. We found that their B-fields are varied, with no single preferred alignment along the entire spine of the bones. At higher column densities, the spines of the bones are more likely to align perpendicularly to the B-fields, although this is not ubiquitous, and the alignment shows no strong correlation with the locations of identified young stellar objects. We estimated the B-field strengths across the bones and found them to be ∼30–150 μG at parsec scales. Despite the generally low virial parameters, the B-fields are strong compared to the local gravity, suggesting that B-fields play a significant role in resisting global collapse. Moreover, the B-fields may slow and guide gas flow during dissipation. Recent star formation within the bones may be due to high-density pockets at smaller scales, which could have formed before or simultaneously with the bones.

Unified Astronomy Thesaurus concepts: Star formation (1569); Interstellar filaments (842); Interstellar magnetic fields (845); Young stellar objects (1834); Polarimetry (1278); Dust continuum emission (412); Protostars (1302); Interstellar dust (836); Dense interstellar clouds (371); Galaxy magnetic fields (604)

1. Introduction

Most stars form within the molecular clouds of a galaxy's spiral arms, and parts of these star-forming clouds are filamentary with widths of ∼0.1 pc (e.g., P. André et al. 2010; A. Hacar et al. 2023). Infrared dark clouds (IRDCs) within the Milky Way have been identified using a variety of telescopes, including the Infrared Space Observatory, the Midcourse Space Experiment, and the Spitzer Space Telescope (e.g., M. Perault et al. 1996; S. D. Price et al. 2001; R. A. Benjamin et al. 2003; R. Simon et al. 2006; S. J. Carey et al. 2009). Among these, some IRDCs were found to be exceptionally elongated, such as Nessie (J. M. Jackson et al. 2010; A. A. Goodman et al. 2014), with large widths of ∼1 pc and lengths ranging from tens to over 100 pc. These structures have been referred to as the "bones of the Milky Way" since they are the densest and largest-scale coherent star-forming structures in the Milky Way (A. A. Goodman et al. 2014). C. Zucker et al. (2015, 2018, henceforth, Z15, Z18) identified 18 such bones, using the criteria that these bones lie mostly parallel and close to the Galactic plane, they are continuous and kinematically coherent, and they have aspect ratios exceeding 20:1. Since stars form in filamentary molecular clouds within spiral arms, studying star formation in these elongated bones provides a detailed view of how mass collects in the magnetized spiral potential to form stars. With the extensive catalog of ancillary data available for these bones, many of their properties, such as length, width, temperature, and density, have been well constrained. However, the magnetic fields (henceforth B-fields) within these bones, which could potentially guide the flow of mass and/or slow the formation of stars, remain poorly constrained.

The most common method for probing B-fields in star-forming clouds is through polarimetric observations of thermal dust emission. Dust grains align with their short axes along the B-field direction, resulting in their long axes being perpendicular to the B-fields (e.g., B.-G. Andersson et al. 2015). Therefore, the thermal emission from these dust grains is polarized in a direction perpendicular to the B-fields. By mapping the polarization direction across an entire region, the plane of the sky direction of the B-fields can be inferred by rotating all the polarization angles by 90°. However, the B-field direction inferred from this method provides only a projected angle on the plane of the sky. By convention, we refer to these angles as B-field "vectors," even though they are not true vectors.

At large scales in the interstellar medium toward Gould Belt clouds, polarimetric observations from Planck have shown that the inferred B-fields tend to be more parallel to low-density elongated structures and more perpendicular to high-density elongated structures (Planck Collaboration et al. 2016). Simulations (J. D. Soler et al. 2013; Planck Collaboration et al. 2016; J. D. Soler & P. Hennebelle 2017) suggest that these observations are consistent with Alfvénic or sub-Alfvénic turbulence, indicating that B-fields are likely to be dynamically important. However, the resolution of these observations was coarse ($10'$ or 0.4 pc for the nearest clouds) and did not resolve the filamentary structure within these clouds. A follow-up higher-resolution observational analysis of a single Gould Belt cloud, L1688, showed that the transition from parallel to perpendicular alignment with increasing column density is consistent with Planck (D. Lee et al. 2021). Galactic bones, which are located much farther away than the Gould Belt clouds, have widths of only a few arcminutes and are therefore not resolved by Planck.

The Stratospheric Observatory for Infrared Astronomy (SOFIA), a Boeing 747SP aircraft equipped with a 2.7 m telescope, was ideal for probing B-fields in bones. Specifically, its polarimeter, the High-resolution Airborne Wideband Camera Plus (HAWC+; C. D. Dowell et al. 2010; D. A. Harper et al. 2018), was well suited for tracing their B-fields because (1) it observed in the far-infrared where thermal dust emission from cold clouds is the brightest, (2) it could resolve the distant bone clouds with large maps, and (3) its sensitivity was sufficient to detect diffuse and dense dust emission. Moreover, as a SOFIA instrument, HAWC+ could target all bones, as they lie in both the northern and southern skies. We utilized SOFIA/HAWC+ for an observational SOFIA Legacy program called FIlaments Extremely Long and Dark: a MAgnetic Polarization Survey (FIELDMAPS), which mapped B-fields for 10 of the 18 bones identified in the Z18 catalog. These 10 bones were selected because they had the most contrast with the background emission from the Galactic plane, allowing for them to be observed in a reasonable amount of time (see S. Coudé et al. 2026; henceforth C25). The first results were published for the G47 bone in I. W. Stephens et al. (2022, henceforth, S22). S22 found that B-fields are not always perpendicular to the G47 bone but tend to be perpendicular in the highest density regions where stars are forming. They also found that B-fields at parsec scales tend to be 20–100 μG, which is strong enough to inhibit gravitational collapse in most of the bone (i.e., subcritical), except possibly in the highest density regions where stars are forming. A separate analysis of G47 FIELDMAPS data by O. R. Jadhav et al. (2025) found similar results in that the energy density of the B-fields dominates over that of turbulence and gravity. N. B. Ngoc et al. (2023) found strong fields (subcritical) toward the Snake bone (also referred to as G11 or G11.11–0.12) using SOFIA data as well, which will be reanalyzed here with an improved data reduction. Analysis of the B-field strengths for all 10 bones will be investigated in this paper.

The data release for the FIELDMAPS survey is given in C25. C25 used both FIELDMAPS and Planck data to analyze the general alignment of fields with the Galactic plane and the large-scale, linear orientation of the bones. The Planck data, which cannot resolve the widths of the bones given the resolution of $5'$ (∼2–8 pc spatial resolution given the varying distances of the bones), showed that B-fields are primarily parallel to the Galactic plane, which is consistent with B-fields following the spiral arms found in both Galactic and extragalactic studies (e.g., D. P. Clemens et al. 2020; A. S. Borlaff et al. 2021). The SOFIA data, on the other hand, showed B-fields that were closer to random, with a very slight overall preference for fields to be perpendicular to the large-scale orientation of the bones, in stark contrast to that found with Planck. This contrast is consistent with the fact that the direction of B-fields in individual star-forming regions shows no dependence on their location within the Galaxy (I. W. Stephens et al. 2011). Since bones exhibit significant curvature and deviate from the linear geometries adopted for simplicity in C25, a detailed analysis of the morphological alignment between B-fields and the bone structure is warranted, which will be investigated in detail in this paper.

This paper extends the analysis of S22 to all 10 bones. In Section 2, we discuss the data used in the paper. In Section 3, we discuss the alignment between B-fields and the spines of the bones and discuss whether this alignment is related to where young stellar objects (YSOs) form. In Section 4, we analyze the effects of gravity and B-fields along the spine of the bone via a sliding box analysis. We discuss the findings in Section 5 and summarize the findings in Section 6.

2. Observations and Ancillary Data

We analyze SOFIA/HAWC+ polarization data from the FIELDMAPS survey in conjunction with ancillary data and parameters estimated in other studies. In the subsections below, we will describe details of the SOFIA observations, column density maps, the bone's spine orientation, molecular line data, and the YSO catalog. Extended details about the FIELDMAPS survey are given in the data release paper (C25).

Table 1 lists the distances to the bones, which were updated in C25 given new Galactic models (M. J. Reid et al. 2019) and maser parallax measurements (Y. W. Wu et al. 2014; J. J. Li et al. 2022). Notably, the Snake, Filament 8, and G47 show substantial changes in their distances compared to Z18. The table also lists the deconvolved full width at half-maximum (FWHM) sizes, as discussed in detail in Z18. The deconvolved FWHM sizes are based on the assumption of a cylindrical geometry for the bones, where Gaussians are fitted to their

Table 1
Bone Parameters and Polynomial Fit Order

Bone Name	Distance[a] (kpc)	FWHM Size[b] (pc)	Radius[c] (pc)	Polynomial[d] Fit Order
Filament 1	4.2 ± 0.3	1.5	1.1	19
Filament 2	3.8 ± 0.4	1.1	0.84	22
Filament 4	4.3 ± 0.5	1.8	1.3	14
Filament 5	4.0 ± 0.4	1.3	0.95	11
Snake[e]	4.1 ± 0.2	1.4	1.0	35
Filament 8	1.3 ± 0.1	0.7	0.46	20
Filament 10	2.9 ± 0.2	1.2	0.84	45
G24	5.3 ± 0.6	1.7	1.3	12
G47	4.2 ± 0.7	1.1	0.83	24
G49	$5.21^{+0.26}_{-0.23}$	1.4	1.0	33

Notes.

[a] Distances are from C25. See C25 for bone coordinates. The distances to the Snake and G49 are derived from water maser parallax measurements (Y. W. Wu et al. 2014; J. J. Li et al. 2022), while the remaining sources use kinematic distances.

[b] Median, deconvolved FWHM widths of the filamentary bones from Z18.

[c] Calculated from the FWHM width using the correction factor from P. A. M. van Hoof (2000).

[d] Polynomial fit order number used to fit the spine of each bone (see Section 2.3).

[e] Also called Filament 6 in Z15; Z18.

radial column density profiles, and the median FWHM value is assigned to each bone. The analysis in this paper needs the radius of the bone, which can be estimated from the FWHM using a correction factor based on an assumed underlying structure and the resolution of the fitted observations (43″ in Z18). We use the correction factor from P. A. M. van Hoof (2000), assuming a disk-like geometry, as fits across the width of "cylindrical" filaments are disk-like. The estimated radii are given in the fourth column of Table 1. The radius for G47 listed here of 0.83 pc differs from the 1.6 pc used in S22, which was based on the Z18 flattening radius from a Plummer fit to the bone, and assumed G47 was at a larger distance.

2.1. SOFIA/HAWC+ Observations

This paper uses Band *E* (214 μm) HAWC+ polarization data from the SOFIA telescope, where we mapped polarization across the 10 bones listed in Table 1. The data primarily come from the FIELDMAPS SOFIA Legacy Program (project code 08_0186; PI: I. Stephens), although data for the Snake are from a combination of programs 05_0206 (PI: T. Pillai) and 06_0027 (PI: I. Stephens). Data presented in N. B. Ngoc et al. (2023) are only from the 06_0027 program. All bones required multiple pointings. Data from 08_0186 used scan mode (on-the-fly mapping), while the data for the Snake used the chop-nod technique. HAWC+'s pipeline uses the `CRUSH` package (A. Kovács 2008a, 2008b), and the imaging modes and calibration are discussed in detail in D. A. Harper et al. (2018). The Level 0 data were reprocessed through the SOFIA data reduction pipeline to create Level 4 products. Details of the FIELDMAPS data reduction process are discussed in-depth in C25, including a comparison between data reduction of chop-nod and scan mode mapping toward a section of Filament 5. The comparison of the mapping modes showed consistency between angles, suggesting that the foreground/background subtraction does not change the polarization morphology. However, when comparing Herschel and HAWC+ data, C25 showed that there is considerable spatial filtering of Stokes *I* data. The analysis of SOFIA data in this paper primarily focuses on polarization angles, which are considered robustly determined and are unaffected by how much we spatially filter Stokes *I*. The native angular resolution of SOFIA/HAWC+ Band E is 18.″2, but the pipeline applies a smoothing of 4.″274, resulting in a final resolution of 18.″7. Given that the distances to the bones vary from 1.3 to 5.21 kpc, the spatial resolution ranges from 0.12 to 0.47 pc, which is sufficient to resolve the radius of each bone.

In general, the HAWC+ maps cover the majority of the dense material in the bones. However, there are a few exceptions where large portions (about half or more) were not completely mapped. Filament 5 was not fully mapped because the eastern part would have been time-prohibitive due to the sensitivity required for that region. Filament 8 was not fully mapped as the SOFIA telescope was decommissioned before the observations could be completed. Additionally, some bones, such as G47, G49, and Filament 10, have their tail ends unmapped, as the required integration times were long relative to the minimal science gain. Nevertheless, the B-fields were mapped across the vast majority of the solid angle covered by these bones.

The HAWC+ instrument uses a rotating half-wave plate to measure the Stokes parameters *I*, *Q*, and *U*. Stokes *I* represents the total intensity (both polarized and unpolarized emission), while Stokes *Q* and *U* parameterize the linear components of the polarization. Typical uncertainties in *I*, *Q*, and *U* varied significantly from bone to bone and within even a bone itself. The polarized intensity, $P_I = \sqrt{Q^2 + U^2}$, has a bias toward positive values since it cannot be negative (J. E. Vaillancourt 2006). This paper uses the debiased polarization fraction following C25:

$$P_{\rm frac} = \frac{\sqrt{P_I - \sigma_{P_I}}}{I}, \quad (1)$$

where σ_{P_I} is the error on the polarized intensity. The error in the polarization fraction is calculated via error propagation

$$\sigma_{P_{\rm frac}} = \frac{P_I}{I}\sqrt{\left(\frac{\sigma_{P_I}}{P_I}\right)^2 + \left(\frac{\sigma_I}{I}\right)^2}, \quad (2)$$

where σ_I is the error on Stokes *I*.

The polarization angle in the plane of the sky is calculated via

$$\chi = \frac{1}{2}\arctan\left(\frac{U}{Q}\right). \quad (3)$$

For the calculation of χ, we used the `arctan2` function in Python, which selects the correct quadrant based on the signs of *Q* and *U*. In this paper, we show the inferred B-field direction, which is χ rotated by 90°, i.e., $\theta_B = \chi + 90°$. θ_B is a position angle measured counterclockwise from the Galactic north. We use data for $P_{\rm frac}/\sigma_{P_{\rm frac}} > 2$ for the majority of our analysis. We choose this threshold rather than $P_{\rm frac}/\sigma_{P_{\rm frac}} > 3$ because our analysis does not depend on individual measurements but rather on an ensemble of polarization data, and statistically, the vast majority of the $2 < P_{\rm frac}/\sigma_{P_{\rm frac}} < 3$ measurements are real detections. As given in C25, the median flux uncertainties for strongly detected polarization vectors ($P_{\rm frac}/\sigma_{P_{\rm frac}} > 3$, $I/\sigma_I > 10$, and $P_{\rm frac} < 30\%$) across each bone varied from 0.04 to 0.24 MJy arcsec^{-2} for Stokes I and 0.055 to 0.30 MJy arcsec^{-2} for Stokes Q and U.

As done in S22, we rotated the equatorial data products into Galactic coordinates using the `reproject` Python package (T. Robitaille et al. 2020) and recalculated the magnetic field position angles following C25. The pixel size of the maps is 4.″55, which is one-quarter of the native 18.″2 resolution. The pixel size differs from the 3.″7 pixel size used in S22. Toward the later SOFIA observation cycles, 4.″55 became the default Band E size in the pipeline and archive, so we opted to use this size for the entire bone sample.

In this work, we assume that B-fields align the grains, and the inferred B-field is perpendicular to the polarization. Radiative alignment torque theory, which is commonly assumed to be the alignment mechanism of grains with the B-field, requires significant radiation to align grains along the B-field (e.g., B.-G. Andersson et al. 2015). Most of the bones have high extinctions even in the infrared due to high column densities, which suggests that grains are aligning only on the surface of the clouds unless there is an internal illuminating source. Determining whether and where the B-field is aligned in clouds requires a careful analysis of the $P_{\rm frac}$ and column density, and such relationships are shown in C25. Nevertheless, such an analysis needs to be nuanced because, for example, B-fields at the highest column densities often exhibit fine substructure, which may be unresolved within a SOFIA beam and would result in a lower value for $P_{\rm frac}$. A deeper analysis of grain alignment in the bones would require modeling that is beyond the scope of this paper. Given these uncertainties about which grains are being aligned along the line of sight, our assumed inferred B-fields are considered the "most likely" direction of the B-field for each SOFIA beam. Since we are analyzing these data primarily in a statistical manner (i.e., many thousands of Nyquist-sampled measurements for each bone; C25), anomalies at particular locations in the bones are not likely to affect the overall results.

An example of the polarimetric map for Filament 1 is shown in the top panel of Figure 1. The bottom panel of this figure shows the line integral convolution (LIC) maps (B. Cabral & L. C. Leedom 1993) for each bone, along with the polynomial fit to the spine (see Section 2.3). The wavy pattern in the LIC map shows the direction of the field morphology, which helps visualize how the field varies along the bone. The polarimetric and LIC maps are shown for the rest of the bones in Appendix A (Figures 8–18). The polarimetric images in this paper are presented slightly differently than in C25, which also used Stokes I contours to highlight the HAWC+ data. Here, the emphasis is on the relationship between B-field vectors, column density, and the bone's spine. Fine details can be seen by zooming in on the figures.

2.2. Column Density Maps

We used column density maps derived from modified blackbody fits of Herschel data from the Hi-GAL program (S. Molinari et al. 2010). Rather than using the Hi-GAL pipeline for deriving column density maps for the bones, as used in S22 (following Z18), here we used the technique described in A. E. Guzmán et al. (2015), which uses a single-temperature modified blackbody dust emission model with an improved background estimation technique that more effectively removes diffuse foreground and background emission. The A. E. Guzmán et al. (2015) model is specifically used to more accurately study these higher-density structures that are often cooler and faint at 70 μm. More details on the column density maps are provided in C25. In this paper, masses M will be calculated from column density N via $M = \mu m_{\rm H} N$, where μ is the mean molecular weight and $m_{\rm H}$ is the mass of a hydrogen atom. We opt to use column density maps of $N_{\rm gas}$ (uses mean molecular weight per particle, $\mu = 2.37$) rather than $N_{\rm H_2}$ (uses mean molecular weight per hydrogen molecule, $\mu = 2.8$) (J. Kauffmann et al. 2008) since $N_{\rm gas}$ is technically the more direct value used for mass calculations. The $N_{\rm gas}$ maps are in Galactic coordinates and have a resolution of 36.″4. For the sliding box analysis used in Section 4, we regrid all the column density maps to have the same pixel size as the HAWC+ maps using `reproject_exact` from the `reproject` Python package (T. Robitaille et al. 2020). Uncertainties in column densities are discussed in A. E. Guzmán et al. (2015), but the assumed gas-to-dust mass ratio of 100 is likely the dominant source of uncertainty.

2.3. Spines and Orientation of Bones

In this paper, we will infer the general orientation of the B-fields and each bone. We follow the method used for G47 in S22. In this approach, the orientation of each bone is determined by fitting a polynomial to its so-called "spine," which is defined in Z18. This spine traces the center of the elongation of the bone of the Herschel column density maps. The spine of the bone was selected using the medial axis skeletonization technique via the `FilFinder` and `RadFil` Python packages (E. W. Koch & E. W. Rosolowsky 2015; C. Zucker & H. H.-H. Chen 2018), which identifies the central part of the bone based on column density contours. The goal in Z18 for these spines was primarily to measure the bone lengths. However, for Filament 5 and Filament 10, this approach did not work for large sections of these bones, as there are places where the bones split into two different filaments. We have since modified the spines for these two bones via `RadFil` to more closely follow the higher-density filament where the bones split, rather than the center of the two combined filaments. The algorithm for the spine skeletonization technique generates a final product of a pixelated Boolean map of the spine's location, with the spine having a width of a single pixel (11.″5 × 11.″5 for Z18).

From the pixelated spine maps, we then fit the spine with a polynomial, as described in S22, so that the orientation of the bone can be determined and compared to the B-field orientation. The order of the fitted polynomials is given in Table 1. The orientation of the bone along the spine is defined by determining the instantaneous slope (i.e., the derivative) of the polynomial at each pixel. In this paper, these orientations along the spine will be referred to as $\theta_{\rm fil}$, and are measured counterclockwise from the Galactic north. The spine maps and their fits will be presented in Section 3.1.

2.4. Molecular Line Data

To calculate the B-field strength and virial parameters along the spine of a bone (Section 4 below), we require knowledge of the velocity dispersion. All the bones lie within the boundaries of several molecular line surveys. Although it is unclear precisely where the polarized dust emission originates (i.e., cloud surface versus the highest density regions; see short discussion on grain alignment in Section 2.1), the polarized

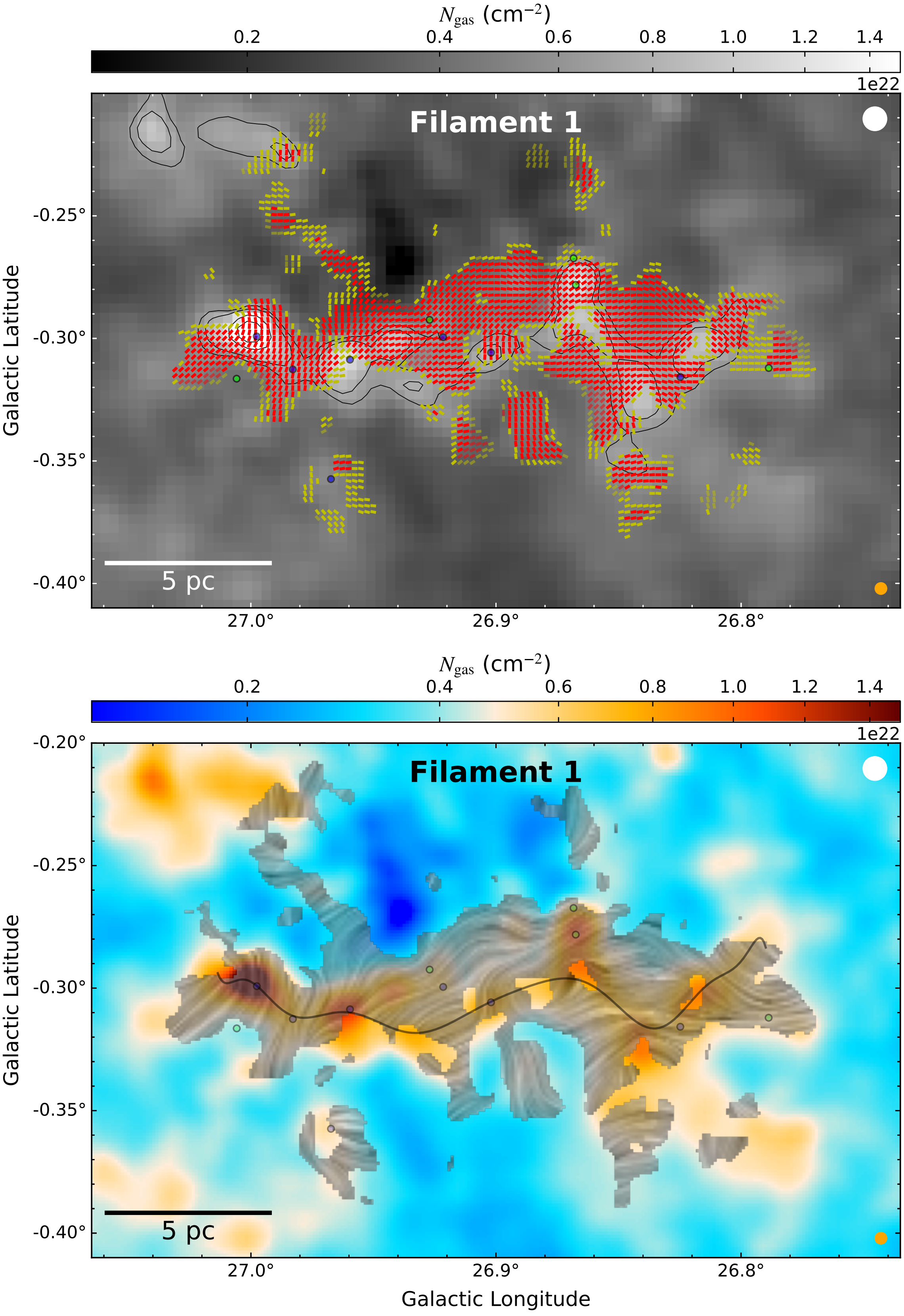

Figure 1. Top panel: Filament 1 inferred B-field vectors overlaid on the Herschel-derived column density map, with contours for this figure and in Appendix A at [0.63, 0.75, 1.3, 1.8, 2.5, 5.0, 7.5] × 10^{22} cm^{-2}. Bright red and yellow vectors have measurements of $P_{\rm frac}/\sigma_{P_{\rm frac}} > 3$ and $2 \leqslant P_{\rm frac}/\sigma_{P_{\rm frac}} \leqslant 3$, respectively; faded vectors indicate where $P_{\rm frac} > 0.15$. Filled blue and green circles mark known Class I and II YSOs, respectively (Section 2.5). Vectors are spaced by 2 HAWC+ pixels (9.″1), near Nyquist sampling. Bottom panel: LIC map overlaid on column density, where the wavy pattern shows the B-field direction for $P_{\rm frac}/\sigma_{P_{\rm frac}} > 1.5$ and $I/\sigma_I > 10$. The spine's polynomial fit is the solid line. The white beam (top right; 36.″4) shows the resolution for the column density map, and the orange beam (bottom right; 18.″7) shows the resolution for SOFIA/HAWC+.

emission almost certainly comes from the bones. As such, for estimating the velocity dispersion, we used spectral lines that are commonly used as high-density tracers, i.e., spectral lines that have high critical densities. In this paper, we use the spectral lines NH_3(1,1), ^{13}CO(1–0), ^{13}CO(2–1), and C^{18}O(2–1), which have similar critical densities (on the order of 10^3 cm^{-3}), which are well suited for tracing the entire bones since their densities are $\sim 10^3$–10^4 cm^{-3}. Spectral lines with higher critical densities will mainly just trace the density peaks. As discussed in R. K. Friesen et al. (2017), NH_3 is an excellent high-density tracer for bones since this gas does not suffer from depletion onto dust grains and is much less likely to be optically thick compared to more abundant molecules like CO.

For six of the more northern bones, we used the high-density tracer ammonia NH_3(1,1) from the RAMPS survey (T. Hogge et al. 2018), which utilized the 100 m Green Bank Telescope (GBT), providing NH_3(1,1) cubes at 32″ resolution. Data for the full RAMPS survey is available via the Green Bank Observatory's website.[20] Using the same spectral setup as RAMPS, we also mapped NH_3(1,1) for G49 under project code GBT23A-288 with the GBT. Observations were taken over 5 days in 2023 May, June, and November. For these observations, we created four overlapping tiles that were scanned using the *K*-band Focal Plane Array (KFPA), and these were sufficient for observing G49 in its entirety. Three of the tiles were 9′ × 9′ and one was 6.′4 × 6.′4 (i.e., about half the area of the bigger tiles), and each tile includes at least one track that was scanned along longitude and latitude. Regardless of the tile size, each tile was scanned for an hour. Before and after each hour scan, we did a pointing and focus with the GBT. The final tile maps were a bit larger than the sizes above, as the KFPA footprint provided noisy edges. We used the GBTIDL pipeline for data reduction and followed T. Hogge et al. (2018) for baseline subtraction. This program involved increased integration time across the bone, allowing for slightly higher NH_3(1,1) sensitivity for G49 compared to the RAMPS survey. The sensitivity of the final maps varied spatially since observations took place on different nights, and some tiles were repeated more than others. The rms noise for the main beam temperature was ~0.3–0.5 K per 0.2 km s^{-1} channel.

While most of the northern bones have almost all of their spine mapped well with NH_3(1,1), Filament 4 and G24 do not; a RAMPS track covering a large part of Filament 4 had exceptionally poor sensitivity, while G24 only had a very small section covered. The lack of high-density tracers for these two bones will be noted throughout the paper.

High-resolution NH_3(1,1) data were not available for Filament 8 and Filament 10. For Filament 8 and Filament 10, we used C^{18}O(2–1) spectral line data from the SEDIGISM survey (F. Schuller et al. 2021) as the high-density tracer. While C^{18}O(2–1) is more likely to suffer from depletion, it is typically not optically thick compared to the more abundant isotopologues of CO. These observations were obtained with the APEX telescope at 30″ resolution and had a channel width of 0.25 km s^{-1}.

Emission from high-density tracers was not detected along the entire length of each bone, primarily due to the limited sensitivity of the surveys. In regions where high-density tracers were not detected, the temperatures are typically warmer and the densities lower. In these lower-density areas, CO is expected to become a suitable alternative for measuring velocity dispersions, as it is less depleted and has lower optical depths as compared to higher-density areas. Accordingly, for these sections, we use the lower-density tracer ^{13}CO, which was available at subarcminute resolution for all bones. The spectral line transition of ^{13}CO was either J = 1–0 (J. M. Jackson et al. 2006) or J = 2–1 (F. Schuller et al. 2021), depending on the available survey. For seven of the bones, we used the Galactic Ring Survey (J. M. Jackson et al. 2006) FCRAO ^{13}CO(1–0) data at 46″ resolution with a channel width of 0.21 km s^{-1}. For the Snake, Filament 8, and Filament 10, we used SEDIGISM ^{13}CO(2–1) data at 30″ resolution and a channel width of 0.25 km s^{-1} (F. Schuller et al. 2021). For the latter two bones, Filament 8 and Filament 10, ^{13}CO(2–1) is largely unused in this paper due to the detection of C^{18}O(2–1) throughout the polarimetric maps. However, we compare the velocity dispersions of the two in Appendix B. The spectral lines and surveys used for each bone for both low- and high-density tracers are also listed in Table 2.

Table 2
Molecular Lines Used to Calculate Velocity Dispersions

Bone Name	Low Density Tracer	High Density Tracer	Surveys
Filament 1	^{13}CO(1–0)	NH_3(1,1)	GRS, RAMPS
Filament 2	^{13}CO(1–0)	NH_3(1,1)	GRS, RAMPS
Filament 4	^{13}CO(1–0)	NH_3(1,1)	GRS, RAMPS
Filament 5	^{13}CO(1–0)	NH_3(1,1)	GRS, RAMPS
Snake	^{13}CO(2–1)	NH_3(1,1)	SEDIGISM, RAMPS
Filament 8	^{13}CO(2–1)	C^{18}O(2–1)	SEDIGISM
Filament 10	^{13}CO(2–1)	C^{18}O(2–1)	SEDIGISM
G24	^{13}CO(1–0)	NH_3(1,1)	GRS, RAMPS
G47	^{13}CO(1–0)	NH_3(1,1)	GRS, RAMPS
G49	^{13}CO(1–0)	NH_3(1,1)	GRS, this study

Note. GRS: Galactic Ring Survey (46″ resolution; J. M. Jackson et al. 2006); RAMPS: Radio Ammonia Mid-plane Survey (32″ resolution T. Hogge et al. 2018); SEDIGISM: Structure, Excitation and Dynamics of the Inner Galactic Interstellar Medium (30″ resolution; F. Schuller et al. 2021).

The spectral lines were fitted for both the high- and low-density tracers as described for G47 in S22 and references therein. In many cases, multiple velocity components were present for a given pixel, which may or may not be associated with the specific bone. We first discarded any velocity component that did not match the bone's systemic velocity given in Z18 since their velocity is either too high or too low to be associated with the bone. If multiple velocity components remained associated with the bone, we selected the velocity component with the highest amplitude as a proxy for the higher-density part of each bone.

For the spectral line fits, the velocity dispersion is crucial for estimating B-field strengths using the Davis–Chandrasekhar–Fermi (DCF) technique described in Section 4. We create a single velocity dispersion map from both low-density and high-density tracers, which will be extensively used in Section 4. In this map, we first regrid all the original velocity dispersion maps to have the same pixel size as the HAWC+ maps with the `reproject` Python package (T. Robitaille et al. 2020), using the function `reproject_adaptive`

---

[20] https://greenbankobservatory.org/portal/gbt/gbt-legacy-archive/ramps-data/

with the parameter `bad_value_mode = "ignore"`. Then, in this map, we use the high-density tracer velocity dispersion when available for a given pixel; otherwise, we use ^{13}CO. Although it would generally be preferable to use a single high-density tracer throughout, as discussed above, high-density tracers are often not detected in parts of the bone with lower column densities. In these regions, the high-density tracer lines are not effectively excited by collisions, making them harder to detect. Nevertheless, as will be discussed in Section 4, when estimating a velocity dispersion in a particular area of a bone, we heavily favor those velocity dispersions measured from the high-density tracer.

A point-by-point comparison of the velocity dispersions along the spine of the bone is presented in Appendix B. The appendix shows that the measured velocity dispersions for low-density tracers are usually higher than high-density tracers, typically by a factor of 2–3. As such, in this paper, we do not analyze in detail the parameters that are measured with low-density tracers (i.e., B-fields, critical ratios, virial parameters, and equilibrium parameters in Section 4).

2.5. *YSOs*

To assess the star formation population across the bones, we use previously identified YSOs from M. Zhang et al. (2019). This survey identified Class I, Flat, and Class II YSOs based on their photometric spectral energy distributions from various Galactic surveys, including data from Spitzer and Herschel. Class 0 YSOs were all combined with Class I YSOs since it is difficult to accurately separate the two based on infrared imaging alone. As was done in M. Zhang et al. (2019), we combine Class I and Flat protostars since this combination represents the embedded protostellar population. Due to the shorter integration times and limited resolution of the Spitzer and Herschel surveys, along with the highly embedded nature of these objects, the catalogs of the youngest YSO populations in the bones are incomplete. Nevertheless, these catalogs provide valuable insights into recent star formation locations within the bones.

The YSOs in the Snake were not originally included in M. Zhang et al. (2019). These YSOs were identified using a method similar to that of M. Zhang et al. (2019), but with the Z18 mask to define the boundary of the Snake.

3. Field Morphology along the Bone

3.1. *Comparing Magnetic Field Orientation, Bone's Morphology, and Density*

C25 analyzed whether or not inferred B-fields are aligned with the bones, based on both Planck and FIELDMAPS HAWC+ observations. The position angle of the bones was fit via a simple linear fit and then compared to the B-field directions. The Planck B-field maps are sensitive to much of the diffuse emission outside of the bones, given their large beam (5′), while the HAWC+ maps are more sensitive to the local magnetic field. For Planck, B-fields are parallel to the elongation of the bones, consistent with B-fields being aligned with the spiral arms. However, for HAWC+, B-fields show a slight preference for being perpendicular to the elongation of the bones, although with a significant variance in orientations locally. Here, we analyze the B-field alignment with each bone more extensively, focusing on how it changes locally along the spine of each bone.

As mentioned before, Figure 1 and those in Appendix A show the inferred B-field direction for each bone from our HAWC+ polarization data. For each bone, there is no single preferred direction of B-fields relative to the bone's morphology. However, at the same time, fields are usually well ordered locally and can have small angle dispersions on scales of several parsecs.

To analyze the general alignment of the B-field orientation with the local morphological direction of each bone, we follow the method described below, which was also used for G47 in S22. In this analysis, we first match the pixel-by-pixel inferred B-field directions (θ_B), as determined from SOFIA/HAWC+ observations, to the nearest spine pixel (see Section 2.3) of the bone. We then take the bone's orientation, $\theta_{\rm fil}$, at this spine pixel and compute the magnitude of the difference, $|\theta_B - \theta_{\rm fil}|$. Figures 2 and 3 show the resulting maps of $|\theta_B - \theta_{\rm fil}|$ for all 10 bones. The color bar is in six discrete bins of 15° each, where bluer colors indicate locations where the B-fields are more parallel to the bone's spine, while redder colors are more perpendicular. In Figures 2 and 3, the B-fields are observed to be a mix of parallel, perpendicular, and everything in between when following the polynomial spine fit for each bone.

While Figures 2 and 3 provide a visual representation of the angle between the spine and the B-field, they do not directly provide a statistical inference of the alignment, nor do they account for the projection of these angles in the plane of the sky. In particular, we are interested in alignment with the filament's spine since the spine tends to have a higher column density where stars are more likely to form. We first extract a subset of the data to analyze only the B-field vectors close to the spine of the bone. We restrict the data to HAWC+ pixels within 23″ (the size of two 11.″5 spine pixels) of the bone's spine, as this distance effectively resolves both the spine and the B-field map. Since bones are at different distances, the analysis traces different physical scales, but this method gives consistency in statistics, given the resolution of the observations. For the analysis of the $|\theta_B - \theta_{\rm fil}|$ distributions below, we consider all HAWC+ pixels in this subset with $P_{\rm frac}/\sigma_{P_{\rm frac}} > 2$.

In S22, visual inspection of G47 indicated that B-fields tend to be more perpendicular at higher densities, with these regions also showing a higher concentration of Class I YSOs. Based on the vector (Figure 1 and Appendix A) and difference maps (Figures 2 and 3), this trend is not readily apparent in the other bones. We will first analyze how the alignment $|\theta_B - \theta_{\rm fil}|$ varies with column density, and then consider the locations of YSOs. The results are plotted in Figure 4. We show $|\theta_B - \theta_{\rm fil}|$ against column density for every other HAWC+ pixel (approximately Nyquist sampled) to capture all the details of the morphology along the spine without excessive oversampling. To help show the general trend of alignment as a function of column density, we divide each plot into 10 equal-sized ranges based on column density,[21] and a box plot is drawn for all data within each range. No box plot is shown if there are fewer than four data points. The box plots show the first and third quartiles in black and the median in orange. For the lowest column density bin where the median of $|\theta_B - \theta_{\rm fil}|$ is above 60° (a preference for perpendicular alignment), we draw a vertical red line. This line helps guide the eye where

---

[21] Points at the minimum and maximum column densities are excluded from the bins due to rounding.

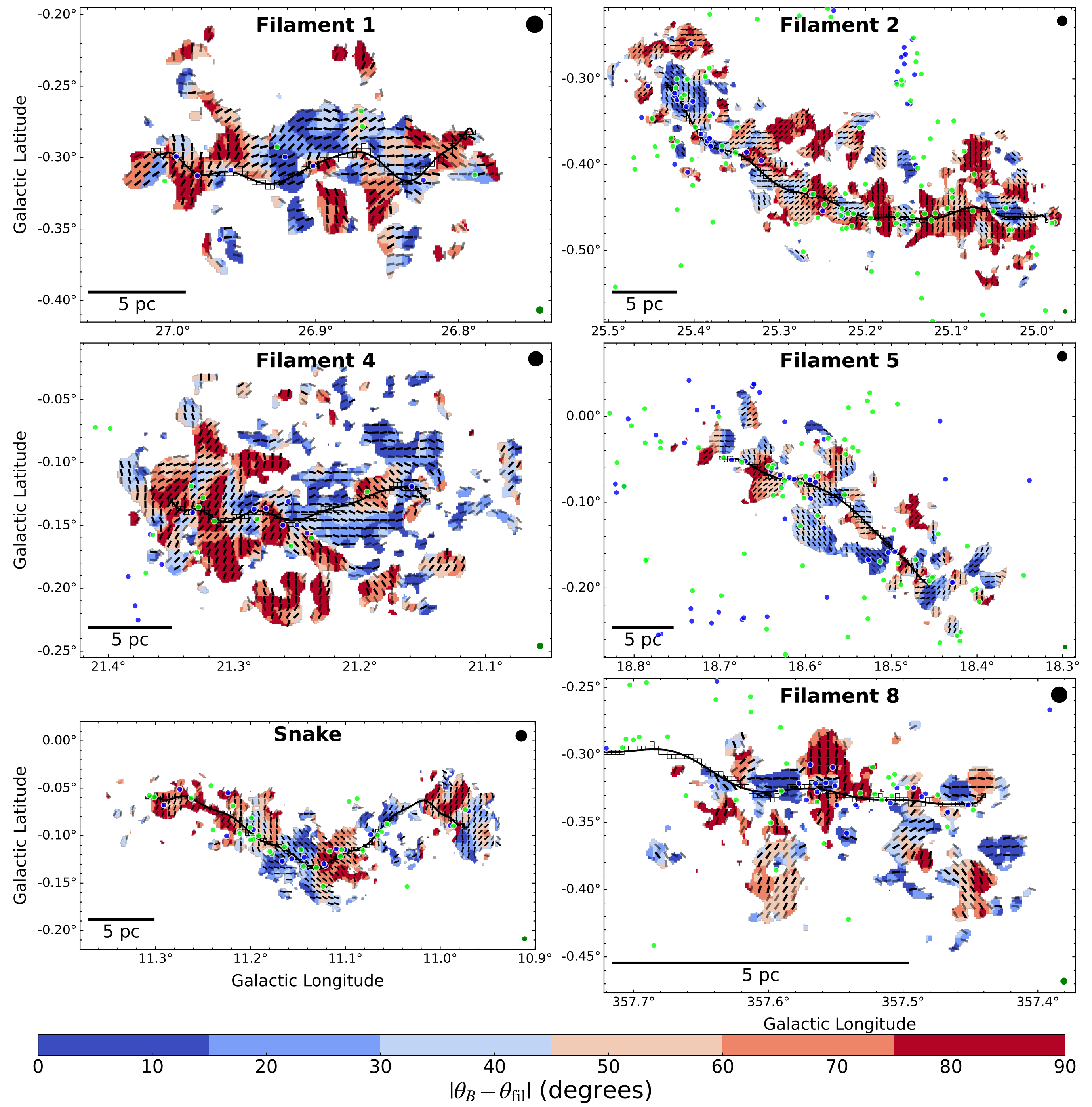

Figure 2. B-field and spine angle difference, $|\theta_B - \theta_{\rm fil}|$, shown in color scale for $P_{\rm frac}/\sigma_{P_{\rm frac}} > 2$ for six of the bones (the other four are in Figure 3). Open squares show the spine pixels of the bones, and the gray line shows the polynomial fit to these pixels (Section 2.3). Black vectors have measurements of $P_{\rm frac}/\sigma_{P_{\rm frac}} > 3$, while faded black (gray) vectors have $2 \leqslant P_{\rm frac}/\sigma_{P_{\rm frac}} \leqslant 3$. Filled blue and green circles show the location of known Class I and II YSOs, respectively (Section 2.5). The black beam on the top right is the column density resolution (36.″4), while the green beam on the bottom right is the SOFIA resolution (18.″7). Vectors are shown are separated by 5 HAWC+ pixels (22.″75 or ∼1.25 beams) to help better visualize the B-field morphology.

perpendicular alignment might transition due to the change in column density.

Based on Figure 4, most bones show a high interquartile range at lower column densities, suggesting that alignment with the bone is random at these column densities. At higher column densities, some bones exhibit a preference for perpendicular alignment between the spine and B-fields. Filament 5 and G47 strongly show this preference, while Filament 1, Filament 2, Filament 4, and the Snake also suggest this preference. In contrast, Filament 8, Filament 10, G24, and G49 do not show a preference for perpendicular alignment at high column densities, with the former two (Filament 8 and Filament 10) even showing a preference for parallel alignment. Since all bones span similar ranges of column densities, these varying preferences indicate that there is no definitive column density at which B-field lines become perpendicular to the bones. This fact is supported by the red vertical line in Figure 4, which occurs at a variety of column densities. Planck

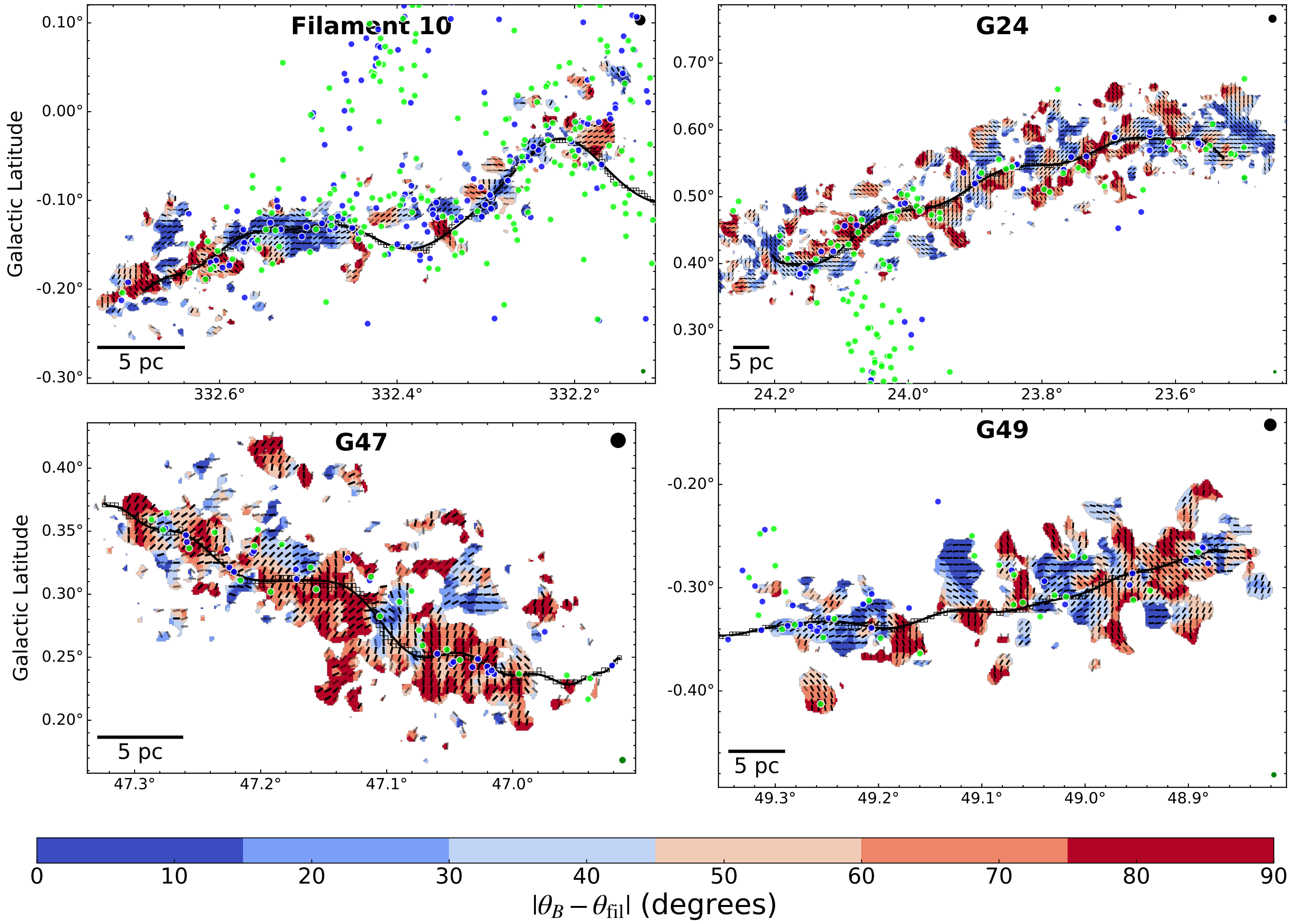

Figure 3. B-field and spine angle difference, $|\theta_B - \theta_{\rm fil}|$, for four of the bones. The caption is the same as that of Figure 2, which shows the other six of the 10 bones.

Collaboration et al. (2016) investigated a similar relationship in 10 nearby star-forming clouds but had a lower spatial resolution (>0.4 pc) and therefore could not resolve filaments (~0.1 pc in size). Instead, their comparison was with dense elongations. They found that most regions preferred B-fields to be parallel to dense elongations at low column densities ($\log(N_{\rm H}[{\rm cm}^2]) \sim 21$–21.5), with either no alignment or a perpendicular preference at higher column densities. The transitory regime from parallel to nonparallel[22] varied among these clouds, with an interquartile range for $\log(N_{\rm H}[{\rm cm}^2])$ of 21.765–22.15. Our observations probe the transitory and higher-density regimes rather than the parallel regime noted by Planck Collaboration et al. (2016). The mix of no alignment and perpendicular alignment at higher densities in nearby star-forming clouds is consistent with our findings for the alignment with the elongation of the bones. However, Filament 8 and Filament 10's preference for some parallel alignment at high column densities was not directly found in Planck Collaboration et al. (2016), possibly because the resolution of Planck (>0.4 pc) is much larger than the widths of the filaments in those clouds (~0.1 pc).

The above analysis does not take into account projection effects. Following previous work (e.g., C. L. H. Hull et al. 2013, 2014; K. I. Lee et al. 2015; see I. W. Stephens et al. 2017 for the methodology we follow), we create a Monte Carlo simulation of a million pairs of random angles on the surface of a unit sphere. From this distribution, we extract angles that are mostly parallel (angle differences $|\theta_B - \theta_{\rm fil}|$ between 0° and 20°) and mostly perpendicular ($|\theta_B - \theta_{\rm fil}|$ between 70° and 90°). We then project all angles onto the plane of the sky to determine the observed angle distributions for mostly parallel, random, and mostly perpendicular cases. In Figure 5, we plot the resulting cumulative distribution functions (CDFs) for $|\theta_B - \theta_{\rm fil}|$ for each bone. The observed distributions are shown in red, and the results of the Monte Carlo simulations are shown in blue. In cyan, we repeat the Monte Carlo simulations, but now we fix the bone in the plane of the sky and randomize the B-field vectors only. We show this because the bones are typically more aligned in the plane of the sky than along the line of sight. Total parallel and perpendicular alignment for the entire bones is likely between the blue and cyan curves.

Since large-scale Galactic B-fields typically trace spiral arms, a bias may exist for B-fields probed by SOFIA to also lie in the plane of the sky. In this case, projection effects would be minimal, producing CDF curves even farther from the blue and cyan curves for parallel and perpendicular. However, the CDFs and data do not show this preference, and B-field directions in star-forming clouds are usually independent of Galactic location (I. W. Stephens et al. 2011). Moreover, C25 showed that the large-scale parallel B-field traced by Planck is very different from the B-fields found with FIELDMAPS. Together,

---

[22] Planck Collaboration et al. (2016) did not find that all regions showed perpendicular alignment, so we use "not parallel" to describe this range.

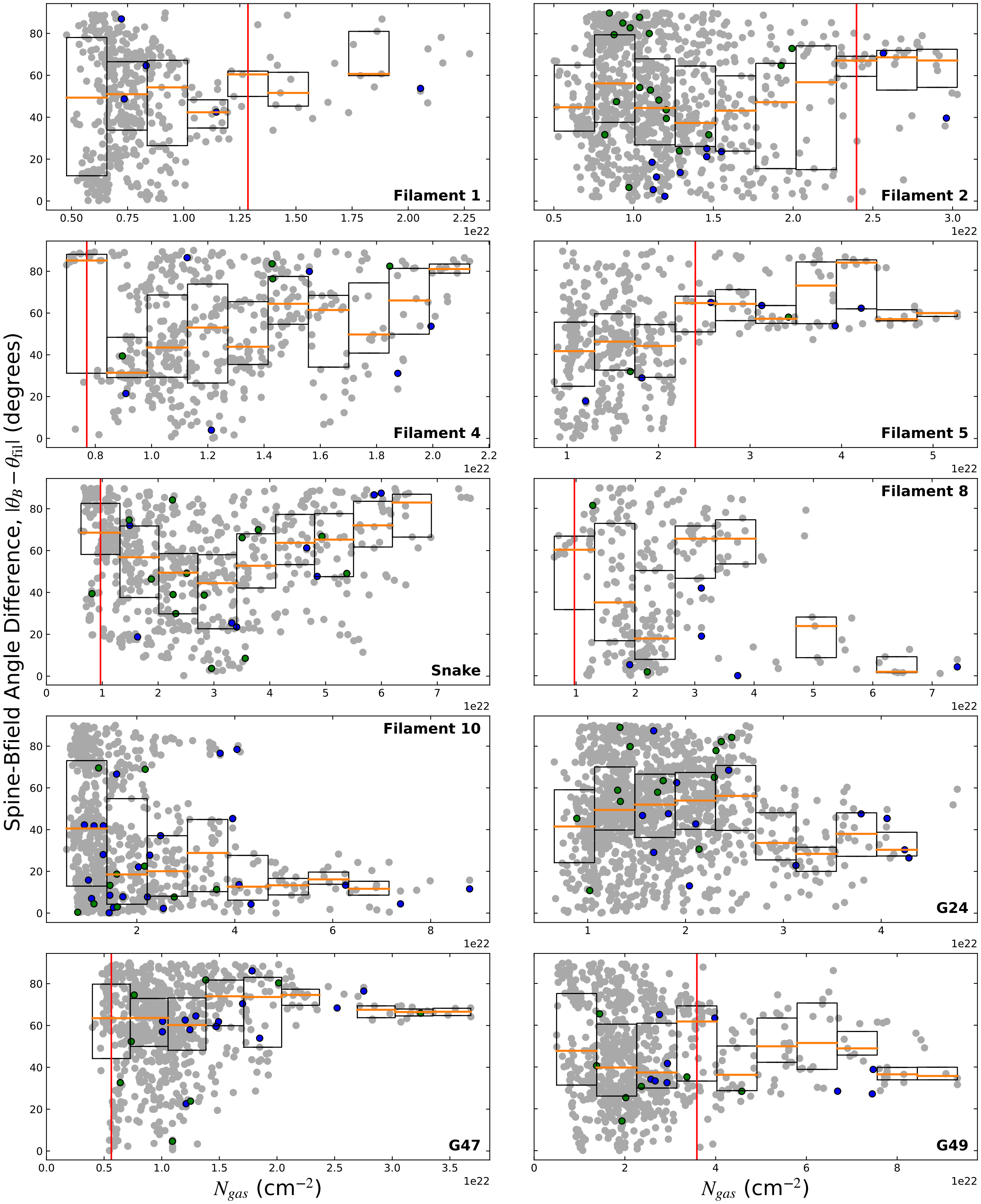

Figure 4. N_{gas} vs. $|\theta_B - \theta_{\mathrm{fil}}|$ for each bone, shown for every other HAWC+ pixel (approximately Nyquist sampled). Only data within 23″ of the bone (two spine pixels) are considered. The data is binned into 10 equal N_{gas} ranges, and box plots are shown if there are at least four points in the bin. The box plots show the first and third quartiles in black and the median in orange. A red vertical line is shown for the first N_{gas} box plot bin where $|\theta_B - \theta_{\mathrm{fil}}| > 60°$, which indicates the first sign of perpendicularity with N_{gas}. Filled blue and green circles show the N_{gas} and $|\theta_B - \theta_{\mathrm{fil}}|$ values at the nearest pixel for the known Class I and II YSOs, respectively.

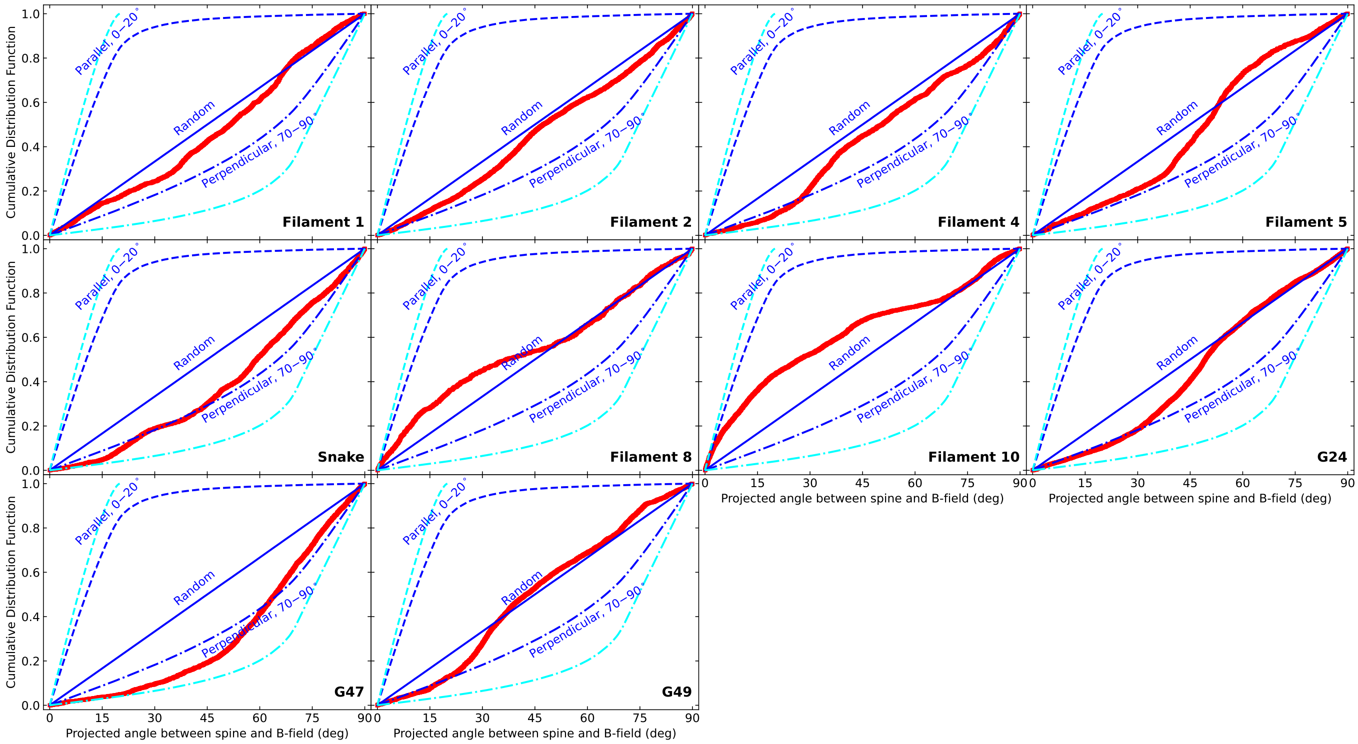

Figure 5. CDF of the angle difference between each bone's spine and B-field direction, $|\theta_B - \theta_{\rm fil}|$. Only pixels within 23″ of the spine are considered. The red line in each panel shows the results for that particular bone. The blue lines in each panel show a Monte Carlo simulation of the expected distribution of projected angles if the spine and B-field directions in 3D are mostly parallel (within 0°–20°; dashed blue line), mostly perpendicular (within 70°–90°; dashed–dotted blue line), or random (solid blue line). The cyan lines show the expected projected angles if the bone is fixed in the plane of the sky for mostly parallel (dashed cyan line) and mostly perpendicular (dashed–dotted cyan line).

these results imply that the most appropriate assumption in the Monte Carlo simulation is that the B-fields are random on the unit sphere.

Based on Figure 5, the B-field vectors do not fit exactly one of the Monte Carlo simulations for parallel, random, or perpendicular alignments. However, the location of the observed CDFs indicates whether B-fields tend to be more parallel or perpendicular compared to random. The alignment of B-fields with the spine is generally more perpendicular than random, especially for G47, whose CDF resembles what would be expected for perpendicular alignment. The two exceptions are Filament 8 and Filament 10, which show a slight tendency to be more parallel. Visual inspection of these two bones in polarimetric maps (Figures 12 and 13) and their difference maps (Figures 2 and 3) reveals that large areas of these bones have projected B-fields that are quite parallel to the bone's spine.

Several bones show features of either being somewhat parallel or perpendicular at the beginning of the CDF, and later converge to be along the random line. Filament 5, Filament 8, Filament 10, G24, and G49 especially show these behaviors. In part, this may be due to the fact that we are looking at a range of column densities. In Appendix C, we show the same CDFs, but now separated into four quartiles based on the column densities at the location of each angle comparison. The results are largely consistent with what is presented in Figure 4, as discussed above.

Furthermore, there may be some bias in the results based on Galactic locations. Based on M. J. Reid et al. (2019), if bones follow spiral arms, the majority of the bones would be mostly in the plane of the sky. The exceptions are G47 and G49, which lie in the Sagittarius-Carina Arm roughly at the tangent point of our line of sight. Given the fact that G47 and G49 have large spatial extents, they may be spurs off the main spiral arms. Moreover, Z15 and Z18 identified Filament 4 and G24 to likely be interarm bones. Overall, our analysis does not find anything substantially different with these spur-like or interarm bones, albeit our sample size in these categories is too small to draw any firm conclusions. Finally, the two bones that have a substantial amount of B-fields that are parallel to the spine, Filament 8 and Filament 10, happen to be the only bones that we observed in Quadrant 4 of the Galaxy. Under the assumption that exactly two of the 10 bones have parallel B-fields assigned at random, the probability that both Quadrant 4 bones (Filament 8 and 10) are parallel, while none of the eight Quadrant 1 bones are is 1/45 (∼2%). However, given that only two Quadrant bones were observed in FIELDMAPS and that Filament 8 was not fully mapped, we cannot make a firm conclusion about a Galactic bias here.

3.2. Bone-field Alignment at Locations of YSOs

We also investigate where the YSOs are forming and whether their locations depend on $|\theta_B - \theta_{\rm fil}|$. First, we examine whether the locations of YSOs correlate with $N_{\rm gas}$. To do this, we compare the typical $N_{\rm gas}$ across each bone to the $N_{\rm gas}$ column density at the locations of Class I and Class II YSOs. We mask out all $N_{\rm gas}$ pixels and YSOs more than 23″ from the spine to focus on regions closest to the bone. For each bone, we calculate the median $N_{\rm gas}$ of the bone and compare it to the median $N_{\rm gas}$ at the exact locations of Class I and Class II YSOs. The results are summarized in Table 3. In all bones, Class I YSOs are more likely to be found at higher $N_{\rm gas}$ values

Table 3
Median Column Densities for Bones and Their YSOs

Bone Name	All N_{gas}	Class I YSOs Total	Class I YSOs N_{gas}	Class II YSOs Total	Class II YSOs N_{gas}
Filament 1	0.72	5	0.83	0	⋯
Filament 2	1.1	10	1.4	18	1.1
Filament 4	1.2	6	1.4	4	1.4
Filament 5	1.5	7	3.1	2	2.6
Snake	2.0	8	4.0	14	2.7
Filament 8	1.8	5	3.1	2	1.7
Filament 10	1.2	24	2.1	10	1.6
G24	1.5	15	2.1	13	1.7
G47	0.87	13	1.5	8	1.2
G49	1.9	9	2.9	7	2.0

Note. All values of N_{gas} are medians and are in units of $\times 10^{22}$ cm^{-2}.

Table 4
Field and Spine Alignment at YSO Locations

Group of Bones	Total YSOs	$\|\theta_B - \theta_{\mathrm{fil}}\|$ >45°	$\|\theta_B - \theta_{\mathrm{fil}}\|$ >60°
All bones, Class I	102	44% ± 5%	29% ± 5%
All bones, Class II	78	56% ± 6%	40% ± 6%
All pixels, all bones	⋯	59.8% ± 0.6%	40.3% ± 0.6%
All perp. bones, Class I	49	61% ± 7%	43% ± 7%
All perp. bones, Class II	46	63% ± 7%	43% ± 7%
All perp. pixels	⋯	63.1% ± 0.8%	43.0% ± 0.8%
Very perp. bones, Class I	20	85% ± 8%	60% ± 11%
Very perp. bones, Class II	10	60% ± 15%	40% ± 15%
All very perp. pixels	⋯	72.2% ± 1.3%	46.8% ± 1.4%

Note. "Total YSOs" indicates the number of YSOs within 23″ of the bone's spine for each particular group. "All perp. bones" includes Filament 1, Filament 2, Filament 4, Filament 5, the Snake, and G47, while "Very perp. bones" include only Filament 5 and G47. For all bones, all perp. bones, and all very perp. bones, we also provide the group's B-field spine alignment statistics for all pixels within 23″ of its spine.

Table 5
Median Percentage of Polarized Light for Column Density Cutoffs

Bone	No Cutoff	$>1 \times 10^{22}$	$>1.5 \times 10^{22}$	$>2 \times 10^{22}$
Filament 1	3.0	2.0	2.0	1.9
Filament 2	3.5	3.1	2.1	1.1
Filament 4	3.7	3.4	3.0	3.4
Filament 5	4.6	4.4	2.9	2.0
Snake[a]	4.2	4.1	4.0	3.9
G24	2.8	2.8	2.5	2.1
G47	3.8	3.3	2.4	2.1
G49	3.4	3.4	2.8	2.5
Filament 8	4.0	3.2	3.6	3.5
Filament 10	3.3	3.1	2.9	2.7

Note. All values are median $P_{\%}$, the percent of light that is polarized across the bone. Only pixels within 23″ of the bone's spine are considered, and every other pixel is skipped. Different cutoffs are based on N_{gas}, with units per square centimeter.

[a] The Snake uses chop-nod, while the rest of the bones are on-the-fly mapping.

than the median N_{gas} for their bone. Class II YSOs also tend to be found at higher N_{gas} values, though not as high as Class I YSOs. The median N_{gas} for Class I YSOs is typically 1.6 times higher than the median N_{gas} for the entire bone, while Class II YSOs are 1.2 times higher. Class I YSOs are generally located in the upper quartile of the column density distribution, whereas Class II YSOs are not. These results suggest that as YSOs evolve, they may migrate away from the bone and/or the bone itself may disperse.

To assess whether or not star formation depends on $|\theta_B - \theta_{\mathrm{fil}}|$, in Figure 4 we plot Class I and Class II YSOs within 23″ of the spine, using their corresponding column densities and $|\theta_B - \theta_{\mathrm{fil}}|$ differences at these locations. No obvious correlation is apparent across all bones. We quantify the frequency of B-field-spine perpendicularity at the locations of Class I and Class II YSOs in Table 4 for three categories: (1) all bones, (2) bones with mostly perpendicular B-fields at high column densities (Filament 1, Filament 2, Filament 4, Filament 5, the Snake, and G47; "all perp. fields"), and (3) bones with very perpendicular B-fields at high column densities (Filament 5 and G47; "very perp. fields"). We evaluate both "any" perpendicularity (angles >45°) and "moderate" perpendicularity (angles >60°). Table 4 also provides the percentages of "any" and "moderate" perpendicularity for all pixels within 23″ of the spine in each of the three groups of bones. These percentages represent the expected values if the YSOs were distributed randomly within each group. The errors for each percentage p are calculated via $\sqrt{p(1-p)/s_n}$, where s_n is the number of YSOs for each subsample.

If YSOs tend to form at locations of perpendicular B-fields, we would expect to see a higher degree of perpendicularity for Class I YSOs compared to Class II YSOs, as younger YSOs should be closer to their birthplace. However, for the entire sample of bones, there is no significant preference for YSOs to form at locations of B-field perpendicularity. In the "all perp. fields" category, there is a slight tendency toward perpendicularity, and this preference is somewhat stronger in the "very perp. fields" category. Despite this, the difference in perpendicularity between Class I and Class II YSOs across all three groups is not statistically significant, showing no more than $\sim 1\sigma$ deviation from random.

These results suggest that YSOs do not show a strong preference for the alignment of B-fields and filaments. YSOs form at high column densities, and if B-fields indicate the direction of gas flow, the location of YSOs is independent of whether the flows are perpendicular or parallel to bones.

3.3. Percentage of Light Polarized along Spines

One potential indicator of the inclination of the magnetic field in the plane of the sky is the polarization fraction P_{frac}. If the magnetic field is in the plane of the sky, dust grains will be maximally polarized, as the long axis of the grain is also in the plane of the sky. On the other hand, if the magnetic field is along the line of sight, the long axis of a spinning dust grain will draw circles in the sky, causing minimal polarization. C25 presents P_{frac} across the entire image for each bone and discusses the results in the context of grain alignment. Here, we focus specifically on the polarization fraction near the bones using the same pixels presented in Figure 4 (i.e., every other pixel and only pixels within 23″ of the bone's spine). Table 5 gives the median polarization percentage, $P_{\%} = P_{\mathrm{frac}} \times 100\%$, for pixels near the bone spine, detected at a 2σ level (i.e., the level used for the sliding box analysis). The statistics of $P_{\%}$ values at lower column densities can suffer from a lack of completeness due to limits on the signal to noise, and they can be artificially inflated due to spatial filtering (see Section 2.1). As such, Table 5 also provides the median $P_{\%}$ values for different column density cutoffs at each pixel.

Median polarization percentages vary from 2% to 4.4% for $N_{\rm gas} > 1 \times 10^{22}$ cm^{-2} and 1.1% to 3.9% for $N_{\rm gas} > 2 \times 10^{22}$ cm^{-2}. The difference in median $P_{\%}$ from bone to bone indicates there could indeed be projection effects of fields in the plane of the sky. However, the median $P_{\%}$ can vary significantly depending on the $N_{\rm gas}$ cutoff, which is especially evident for Filament 2 and Filament 5. We also caution interpreting the larger values for the Snake in the context of the other bones, as the mapping strategy (chop-nod) was different for this bone.

Besides magnetic field projection effects, there are numerous factors that can also affect the observed polarization fractions calculated for each bone. Among these are grain alignment efficiency, spatial filtering for the telescope, beam averaging, optical depth effects, confusion along the line of sight, and stellar feedback (e.g., outflows). Beam averaging is especially complex, as the bones are at varying distances, and fields are likely more complex at smaller scales, especially for the highest column densities. Moreover, there is likely some low-level $P_{\%}$ that are below our 2σ cutoff for this analysis, which may reduce the median $P_{\%}$ for some of the bones. Due to these confounding variables, a general conclusion about the inclination of the magnetic field is an exceedingly difficult task, beyond the scope of this paper. However, what can be said is that $P_{\%}$ does not vary greatly from bone to bone, meaning it is unlikely that severe projection effects across the entirety of bones are causing a significant effect on the overall conclusions of this paper.

4. Magnetic Field and Virial Estimates via Sliding Box Analysis

In this section, we analyze the relative importance of magnetic fields and gravity in the bones using a sliding box analysis similar to that of S22. In short, we slide a box along the spine of each bone and estimate the average B-field strength within this box, and evaluate its importance compared to gravity via the critical ratio λ. Additionally, we compute the virial parameter, $\alpha_{\rm vir}$, and combine it with λ to evaluate the potential for collapse within the bone.

4.1. Sliding Box Method

We calculate the B-field of each bone following the sliding box procedure outlined for G47 in S22, with some modifications. We slide a rectangular box along the spine of each bone and compute the magnetic B-field for the box using the DCF technique. This box has a length and width of about 4 and 3 HAWC+ beams ($72\farcs8 \times 54\farcs6$, or 16×12 HAWC+ pixels), respectively, which is similar to but slightly different from the dimensions used in S22 due to differences in pixel size (see Section 2.1). On a spatial scale, the box size corresponds to approximately 0.5 pc × 0.35 pc for the closest bone (Filament 8) and 1.8 pc × 1.4 pc for the farthest bone (G49). This box size was chosen so that there are enough beams to provide a sufficient determination of the angle dispersion. Specifically, the rectangular area of the box divided by the circular area of the HAWC+ beam (assuming the radius is half the FWHM) is 14.5. Given that our underlying assumption when using the DCF technique (discussed below) is that the unperturbed B-field is uniform, we do not use a larger box as the uniform B-field assumption becomes less accurate. The rectangular box is aligned along the spine, and we slide it by one spine pixel ($11\farcs5$; see Section 2.3) at a time. The angle of the box along the spine is determined from the instantaneous slope of the polynomial fit of the spine of each bone, $\theta_{\rm fil}$ (Section 2.3). Details on which pixels fall within a tilted box are provided in the appendix of S22.

Within each rectangular box, we calculate the plane of the sky B-field strength using the modified DCF technique from E. C. Ostriker et al. (2001):

$$B_{\rm pos} = Q\sqrt{4\pi\bar{\rho}}\,\frac{\delta v_{\rm los}}{\delta\theta}, \tag{4}$$

where Q is a projection factor (taken to be 0.5; E. C. Ostriker et al. 2001), $\bar{\rho}$ is the mean density, $\delta v_{\rm los}$ is the line-of-sight velocity dispersion, and $\delta\theta$ is the angle dispersion within the box. Typical median $\delta v_{\rm los}$ for each sliding box measured for NH_3(1,1) vary slightly from bone to bone, from ~0.4 km s^{-1} to 1 km s^{-1}. Although $\delta v_{\rm los}$ technically refers to the nonthermal component alone, we do not subtract the thermal component in this analysis as it is negligible; the temperatures of these bones are usually less than 20 K (C25), implying thermal velocity dispersions of <0.1 km s^{-1}. S22 used the R. Skalidis & K. Tassis (2021) version of the DCF technique, but we opt to use the E. C. Ostriker et al. (2001) version because it is used more frequently and can be more directly compared to other studies. Additionally, the statistical estimates from E. C. Ostriker et al. (2001) exhibit smaller deviations from corresponding simulation estimates compared to the R. Skalidis & K. Tassis (2021) study (P. C. Myers et al. 2024). The B-field strength estimate from R. Skalidis & K. Tassis (2021) differs from E. C. Ostriker et al. (2001) by a factor of $\sqrt{2\delta\theta}$, where $\delta\theta$ is in radians. Consequently, our B-field estimates in regions with lower angular dispersion may be up to a factor of ~2 larger than the R. Skalidis & K. Tassis (2021) version of the DCF technique.

The value for $\bar{\rho}$ in each box is calculated from the $N_{\rm gas}$ maps following the appendix in S22, which assumes bones are cylindrical with radii provided in Table 1. For calculating $\bar{\rho}$, we specifically use the median value of $N_{\rm gas}$ in the box as it removes potential outliers without considerably changing it from the mean value (S22). To determine $\delta v_{\rm los}$, we take the velocity dispersion maps discussed in Section 2.4, which may be (and often is) a mix of low- and high-density tracers. If 39 (which corresponds to ~20%) of the 16×12 sliding box pixels have a valid fit with a high-density tracer (equivalent to the area of a circle with a RAMPS beam's FWHM as the diameter), we take the median velocity dispersion of the high-density tracer only. Otherwise, we take the median of the mix of low- and high-density tracers. We find that if we do not use the 39 pixel criterion, there are several instances where the low-density tracer provides excessively high-velocity dispersions compared to the low-velocity dispersions, causing large $B_{\rm pos}$ that we believe are likely not as accurate.

The intrinsic standard deviation, $\delta\theta$, is affected by observational errors. Many studies correct for the intrinsic dispersion via $\delta\theta = \sqrt{\delta\theta^2_{\rm obs} - \sigma^2_\theta}$ (e.g., J. M. Girart et al. 2006; R. Rao et al. 2009; I. W. Stephens et al. 2013), where $\delta\theta_{\rm obs}$ is the standard deviation of angles in the box, and σ_θ is the observational error. This methodology was used for G47 in S22. However, this formula assumes that the telescope beam does not significantly smooth out the intrinsic angle dispersion within the box. Whether HAWC+ significantly does this or not is unclear, but we suspect that since we are estimating the dispersion of a larger-scale field within the box, this effect is not large. The correction also assumes all errors are Gaussian. For this study, we assume that $\delta\theta = \delta\theta_{\rm obs}$ rather than applying the correction. We choose not to correct for two reasons: (1) we want to avoid potentially overestimating the B-field, and (2) there are many locations where the field is quite structured, and σ_θ happens to be larger than $\delta\theta_{\rm obs}$; such a result implies these are statistical anomalies or the observational errors of HAWC+ are overestimated. In general, we find that applying the correction has a minimal effect on the median B-field strength across the bone for the sliding box analysis, typically increasing the strength by less than 10%.

To calculate the importance of B-fields compared to gravity, we determine the critical ratio, λ, which compares the observed mass-to-flux ratio with the mass-to-flux ratio required for gravitational collapse, as described by (R. M. Crutcher et al. 2004):

$$\lambda = \frac{(M/\Phi)_{\rm obs}}{(M/\Phi)_{\rm crit}}, \tag{5}$$

where $(M/\Phi)_{\rm crit}$ is assumed to be $1/(2\pi\sqrt{G})$ (C. F. McKee & E. C. Ostriker 2007). In the context of the sliding box analysis, as outlined in the appendix of S22, we consider the 3D geometry of the sliding box, which is modeled as a cutout of the cylindrical bone. The direction of the B-field is taken as the median angle within the sliding box, and the B-field is assumed to be inclined in the sky by the statistical average of 38.°2 (R. M. Crutcher et al. 2004).

We also calculate the virial parameter within each sliding box using the cylindrical formulation of the virial parameter (P. S. Li et al. 2022), which is

$$\alpha_{\rm vir} = \frac{2\delta v_{\rm los}^2}{GM_l}, \tag{6}$$

where $\delta v_{\rm los}$ is again the line-of-sight velocity dispersion (determined the same way it was for $B_{\rm pos}$ above), and M_l is the mass per unit length of the bone within the box. The mass within the box is computed from the box size and $N_{\rm gas}$ maps, assuming a mean molecular weight of $\mu_p = 2.37$ (J. Kauffmann et al. 2008). M_l is simply this mass divided by the length of the box. An ideal, long cylindrical filament can be supported against collapse if $\alpha_{\rm vir} > 1$.

We then calculate what we call the "equilibrium index," ϵ, which accounts for the fact that in order for a cloud to collapse, it must not only have gravity dominating over the B-fields but also sufficient gravity to overcome other forms of support. The equilibrium index is defined as

$$\epsilon = \sqrt{\lambda^{-2} + \alpha_{\rm vir}^2}\,. \tag{7}$$

An ideal, long cylindrical filament is supported against collapse by a B-field and thermal/turbulent motions if $\epsilon > 1$ (P. S. Li et al. 2022).

The results of the sliding box analysis for each bone are shown in Figure 6. For each bone, there are four panels, which show $B_{\rm pos}$, λ, $\alpha_{\rm vir}$, and ϵ along the bone's spine, with the color scale showing the values. If a point has a black forward slash, the parameter was estimated using low-density tracers.

In the panels for $B_{\rm pos}$, λ, and ϵ, points that are black in their entirety indicate where the angle dispersion $\delta\theta > 25°$, as the DCF technique no longer applies in these cases (E. C. Ostriker et al. 2001). At these locations, (1) the turbulence may be super-Alfvénic, (2) the box is at a location where there is a transition of two distinct B-field morphologies, and/or (3) the assumption of a uniform field is poor. White points mark locations with a limited number of significant B-field vectors in the box. Specifically, these are areas where less than 70% of the box has vectors detected at a 2σ level, or less than 30% of the box has vectors at a 3σ level. Notably, for some extended regions of the bones, such as Filament 8 and Filament 10, large areas were not mapped, resulting in a considerable number of white points. The panel showing $\alpha_{\rm vir}$ does not have white or black points since it is independent of the B-field morphology. Lastly, some areas along the spine are blank due to difficulties in accurately fitting a well-constrained velocity dispersion to any pixels within the box. These blank regions are infrequent but are most apparent on the western (right) side of Filament 1.

Table 6 further quantifies the range of each sliding box parameter, reporting the median and interquartile range (i.e., 25th and 75th percentiles) of the data used in the sliding box analysis. For all parameters, we only report values where we have a valid B-field strength that was estimated using the velocity dispersion of a high-density tracer. Note that some of the median $\alpha_{\rm vir}$ values reported here differ from those reported in Figure 6 because the medians in the figure include $\alpha_{\rm vir}$ values measured at locations with no B-field measurements. As seen, B-field measurements tend to be about 30–150 μG, λ and $\alpha_{\rm vir}$ are $\sim$0.5, and ϵ is $\sim$2. Filament 8 and 10 have higher $\alpha_{\rm vir}$, which is likely due to using $C^{18}O(2–1)$ as the high-density tracer, which probably overestimates the velocity dispersion.

4.2. Analyzing the Sliding Box Results

Here, we analyze the sliding box results of Figure 6 more thoroughly. To assist with the interpretation, we first review key aspects and limitations of the sliding box approach. First, each value along the spine represents an average within the rectangular sliding box, which is rotated to align with the spine. The size of the box is 72.″8 × 54.″6 (16 × 12 HAWC+ pixels), providing a consistent angular scale, but the spatial scales vary due to the differing distances of the bones. Therefore, comparisons between bones should consider the different spatial extents probed for each bone. In many regions, the B-field strengths could not be estimated, mainly due to excessive angular dispersion ($\delta\theta > 25°$) or insufficient B-field data. These regions could be potential locations where B-field strengths are low and thus more easily tangled, but they can also be places where there are multiple B-field components within each box along the line of sight and/or the plane of the sky. These regions could also be locations where most of the B-field is along the line of sight. Moreover, we primarily focus on measurements that are derived from velocity dispersions of the high-density tracers, as the ones from low-density tracers are likely overestimated (see Appendix B). G24 and Filament 4 have very few velocity dispersions measured with high-density tracers.

Additionally, there are significant uncertainties arising from assumptions such as bone geometry, diffuse emission, the

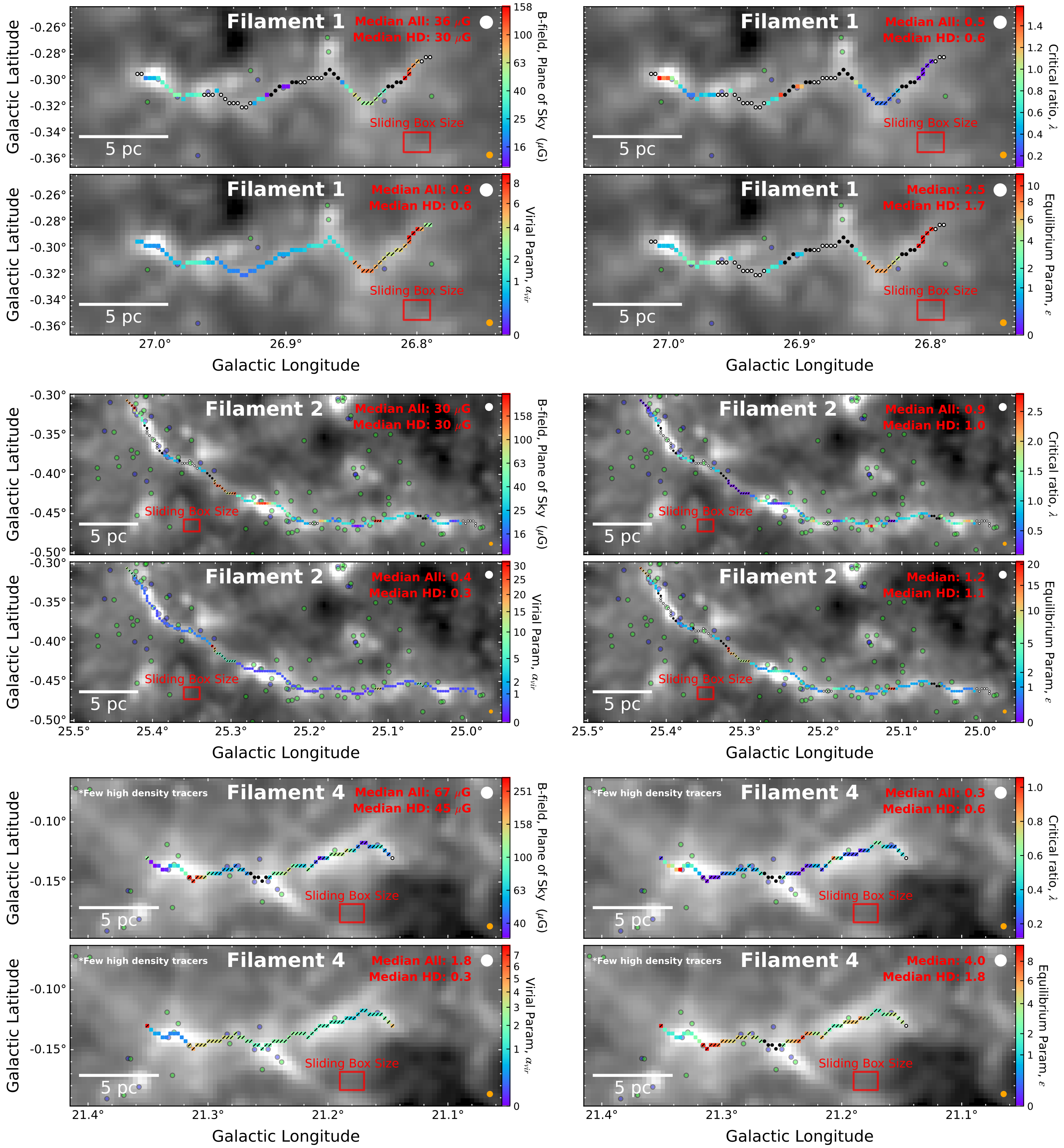

Figure 6. Sliding box results for each bone, where $B_{\rm pos}$, λ, $\alpha_{\rm vir}$, and ϵ for the sliding box along the spine are shown in color scale, and the gray scale shows the gas column density, $N_{\rm gas}$. Color scales for λ is a linear scale, while the others are on a square root scale. A black forward slash "/" through a point indicates that the velocity dispersions are likely overestimated, as they were measured with a low-density tracer (see Section 2.4). Black and white points are locations where we were unable to make estimates (see the text). The box size is shown in each panel, which was allowed to rotate as it slid across the spine. The top right of each panel shows the median for all points and for those using only high-density (HD) tracers. Figure 1 gives the beam sizes, and Figure 1 and the figures in Appendix A quantify the gray scale for each bone.

choice of the DCF method, and the assumption of a uniform B-field. These factors cause considerable difficulty in determining accurate B-field uncertainties at each location, and thus, we do not explicitly estimate them in this paper. The B-field strength and λ estimates could be off by a factor of 2 or even 3. Some of the factors may cause an overestimate of the B-field strength (e.g., beam smearing of polarization and kinematic data), while other assumptions may cause an underestimate of the B-field strength (e.g., assumed uniform structure in each box and not correcting for observational

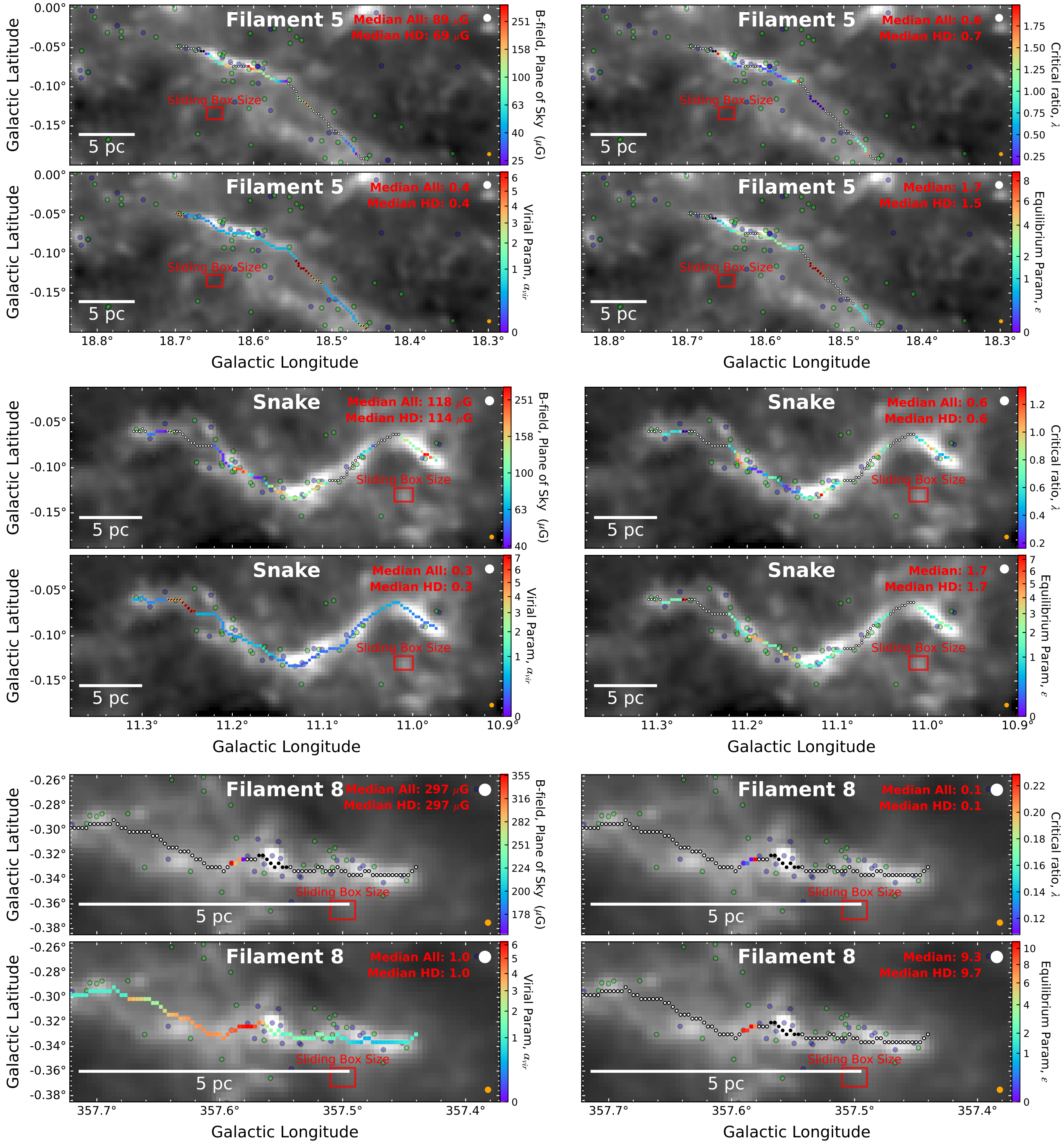

Figure 6. (Continued.)

errors). Because of these confounding factors, it is difficult to ascertain whether B-fields are generally overestimated or underestimated. However, the errors due to the assumptions are at least somewhat correlated, which allows us to make valid comparisons of the relative field strengths between bones and along the spines of each bone itself.

To gather a general sense of the values across all figures, in Figure 7, we plot all $B_{\rm pos}$, λ, and $\alpha_{\rm vir}$ as a function of number density, $n_{\rm gas}$, which complements the information presented in Figure 6. For Figure 7, we will focus the discussion primarily on the filled circles, as these have more accurate velocity dispersions measured by high-density tracers. Across the bones, most B-field strengths along the spine are a few tens of microgauss to a few hundred microgauss. The largest estimated B-fields are for G49, which reach almost 1 mG. A weak but positive correlation is found between number density and volume density. This topic will be further explored in Section 5.

The critical ratio, λ, is typically found to be less than 1, indicating that B-fields are generally strong enough to

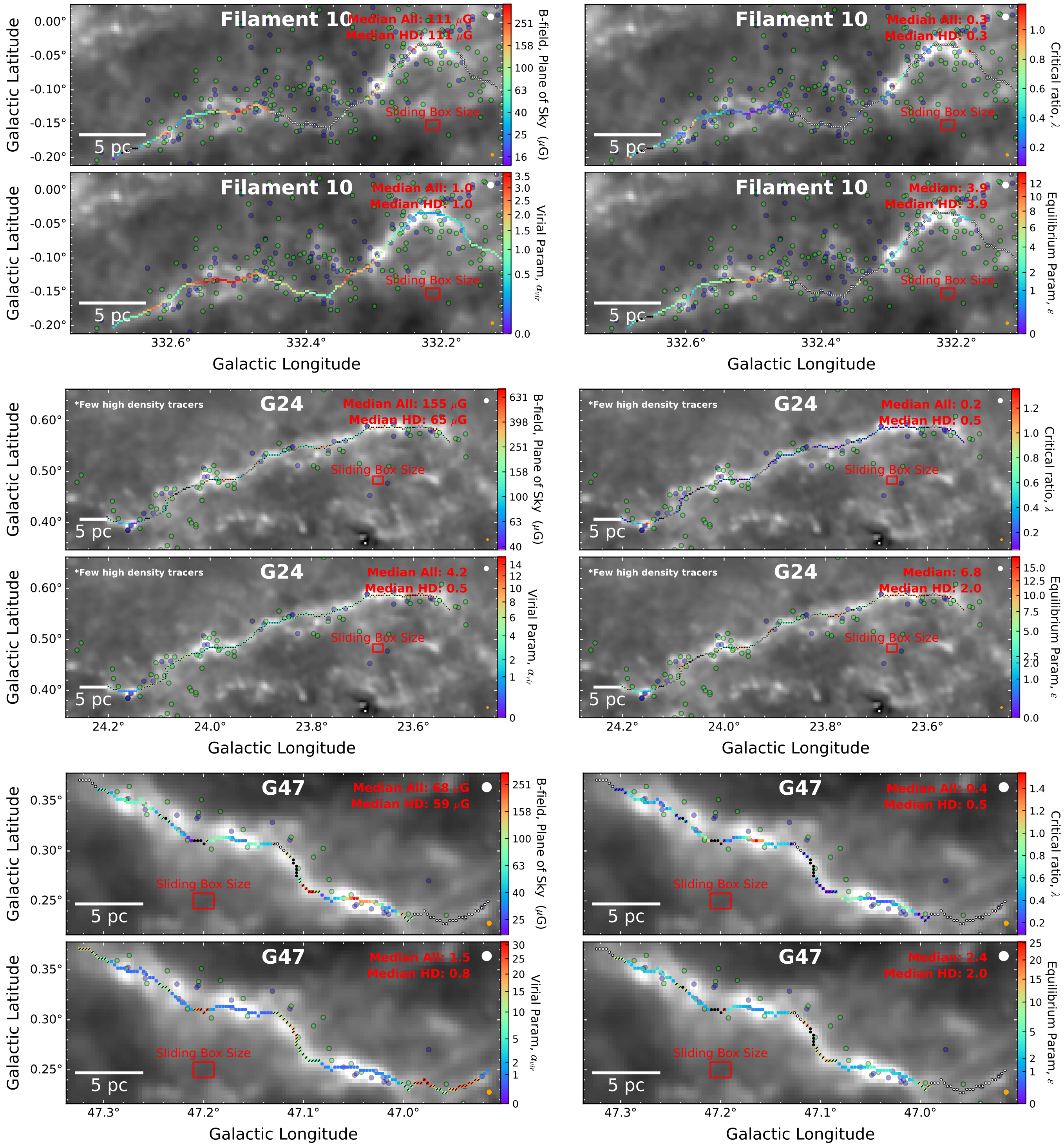

Figure 6. (Continued.)

counteract gravitational collapse in the bones. In most cases, λ is 0.5 or less, and values of $\sim$0.2 are not atypical. Even if λ is underestimated (e.g., by overestimating B_{pos}), the B-fields are still likely playing a significant role in supporting the bones against gravitational collapse. Critical ratios appear to be independent of volume density.

As measured by the high-density tracers, virial parameters are almost always less than 2, indicating they are at least self-gravitating, but they are usually even less than 1, which indicates collapse in the absence of B-fields. The only exceptions are Filament 8 and Filament 10, but these virial parameters are likely overestimated due to using $C^{18}O(2–1)$ as the high-density tracer rather than $NH_3(1,1)$ (see Appendix B). Since Filament 8 and Filament 10 likely have overestimated velocity dispersions, they likely have overestimated B-field strengths as well. Finally, the virial parameters as measured by low-density tracers do have virial parameters often much more than 2. While their velocity dispersions are likely overestimated, some calculations exceed 10, indicating there may be portions of the bones that are unbound.

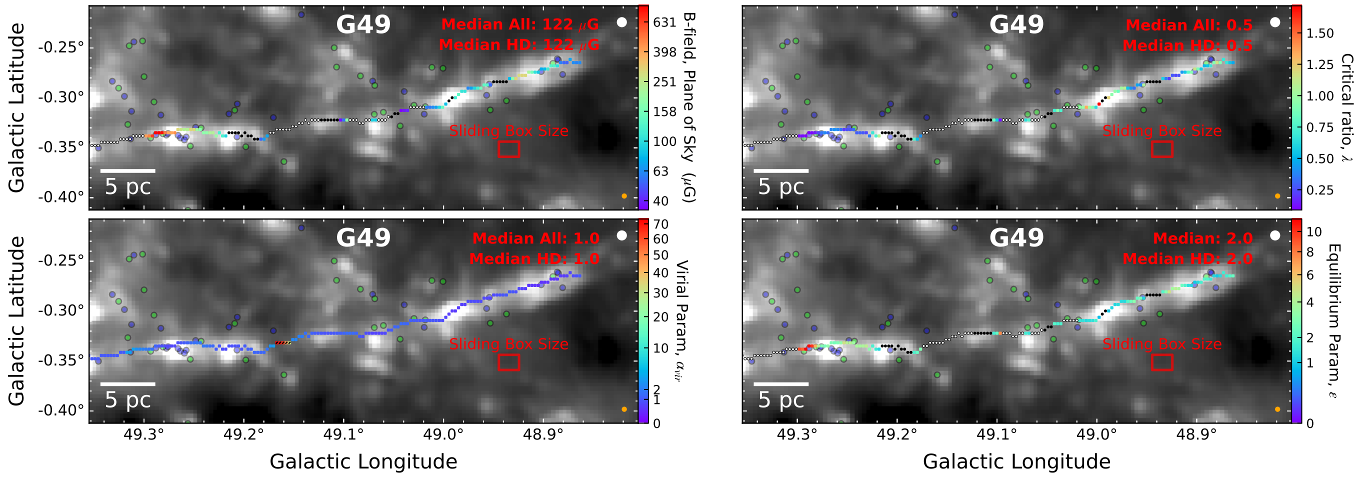

Figure 6. (Continued.)

Table 6
Sliding Box Parameters with High-density Tracer and B-field Measurements

Bone Name (1)	Total Count (2)	$n/1000$ (cm^{-3}) (3)	$\delta v_{\rm los}$ (km s^{-1}) (4)	$B_{\rm pos}$ (μG) (5)	λ (6)	$\alpha_{\rm vir}$ (7)	ϵ (8)
Filament 1	24	$1.1^{(1.4)}_{(1.0)}$	$0.49^{(0.63)}_{(0.39)}$	$30^{(36)}_{(22)}$	$0.6^{(1.1)}_{(0.5)}$	$0.5^{(1.2)}_{(0.4)}$	$1.7^{(2.5)}_{(1.1)}$
Filament 2	94	$2.3^{(2.7)}_{(2.0)}$	$0.39^{(0.48)}_{(0.34)}$	$30^{(38)}_{(22)}$	$1.0^{(1.3)}_{(0.8)}$	$0.3^{(0.4)}_{(0.3)}$	$1.1^{(1.5)}_{(0.8)}$
Filament 4	10	$2.1^{(2.3)}_{(1.7)}$	$0.47^{(0.47)}_{(0.46)}$	$45^{(76)}_{(35)}$	$0.6^{(0.8)}_{(0.4)}$	$0.3^{(0.3)}_{(0.3)}$	$1.8^{(2.4)}_{(1.4)}$
Filament 5	33	$3.0^{(3.9)}_{(2.9)}$	$0.54^{(0.62)}_{(0.52)}$	$69^{(119)}_{(37)}$	$0.7^{(1.1)}_{(0.4)}$	$0.4^{(0.5)}_{(0.3)}$	$1.5^{(2.8)}_{(1.0)}$
Snake	67	$4.0^{(6.4)}_{(2.7)}$	$0.53^{(0.59)}_{(0.48)}$	$114^{(147)}_{(53)}$	$0.6^{(0.8)}_{(0.5)}$	$0.2^{(0.3)}_{(0.2)}$	$1.7^{(2.2)}_{(1.2)}$
Filament 8	4	7.7	1.25	297	0.1	5.2	9.7
Filament 10	92	$2.9^{(4.2)}_{(2.2)}$	$1.01^{(1.15)}_{(0.75)}$	$111^{(166)}_{(61)}$	$0.3^{(0.5)}_{(0.2)}$	$1.9^{(2.8)}_{(1.2)}$	$3.9^{(5.6)}_{(2.3)}$
G24	14	$1.9^{(2.7)}_{(1.5)}$	$0.74^{(0.78)}_{(0.67)}$	$65^{(83)}_{(47)}$	$0.5^{(1.1)}_{(0.4)}$	$0.5^{(0.6)}_{(0.4)}$	$2.0^{(2.4)}_{(1.1)}$
G47	67	$2.3^{(3.2)}_{(2.0)}$	$0.65^{(0.76)}_{(0.61)}$	$59^{(79)}_{(40)}$	$0.5^{(0.8)}_{(0.4)}$	$0.8^{(1.0)}_{(0.6)}$	$2.0^{(2.6)}_{(1.7)}$
G49	79	$3.7^{(5.1)}_{(3.2)}$	$1.01^{(1.29)}_{(0.84)}$	$122^{(230)}_{(70)}$	$0.5^{(0.9)}_{(0.3)}$	$0.8^{(1.2)}_{(0.6)}$	$2.0^{(3.4)}_{(1.4)}$

Note. Statistics for each parameter are reported only at locations with valid B-field measurements where a high-density tracer was used to calculate the velocity dispersion, with the total sample count listed in Column (2). The table also includes the volume density n and $\delta v_{\rm los}$ used for each measurement in the sliding box analysis. Columns (3)–(8) give the median values of each parameter, with superscript and subscript values indicating the upper and lower quartiles (25th and 75th percentiles), respectively. Quartiles are not reported for Filament 8 due to its small sample size.

Despite the low virial parameters, the strong B-fields caused the bones to have ϵ values above 1, indicating that B-fields are helping to support them against collapse, even when the virial parameter is small. Only Filament 2 has a substantial portion of its bone with ϵ below 1. Filament 2, which already has a large population of YSOs, is likely to continue to collapse and form additional stars. Given the uncertainties, it is possible that other bones have parts likely to collapse, but nevertheless, B-fields likely play a significant role. Moreover, high $\alpha_{\rm vir}$ values are often found in the presence of strong B-fields ($\lambda < 1$), which may suggest that B-fields may be important for the dissipation of bones, which will be discussed more in Section 5.

Given that YSOs have been identified toward these bones, despite these high B-field strengths, there has been a history of star formation, and a reasonable assumption would be that star formation would continue in the future. To determine the approximate sliding box parameters ($B_{\rm pos}$, λ, $\alpha_{\rm vir}$, and ϵ) at the location of each YSO, we first match each YSO to the nearest sliding box pixel. We only consider YSOs within 23″ of the bone's spine and that have a valid B-field strength as measured by a high-density tracer. For each bone, we then take the median value of all the YSO-matched sliding box results, which are presented in Table 7. The results are separated into all Class I and II YSOs, Class I by themselves, and Class II by themselves. There is no obvious difference in the sliding box results for Class I versus Class II results, which is partially due to the low number of statistics. Moreover, when comparing the YSO results to the sliding box results across the entire bones (Figure 6), the medians in general are similar. These results thus suggest no correlation between YSO location and the sliding box results.

5. Discussion

In Section 4, we find evidence that magnetic fields are important for the collapse and perhaps the dissipation of the bones. The critical ratio λ is typically much less than 1, and even given the large uncertainties in B-field measurements, the bones appear mostly subcritical. Moreover, low $\alpha_{\rm vir}$ values suggest that much of the bones would collapse in the absence of B-fields. However, there are some low-density locations of the bones that may be unbound.

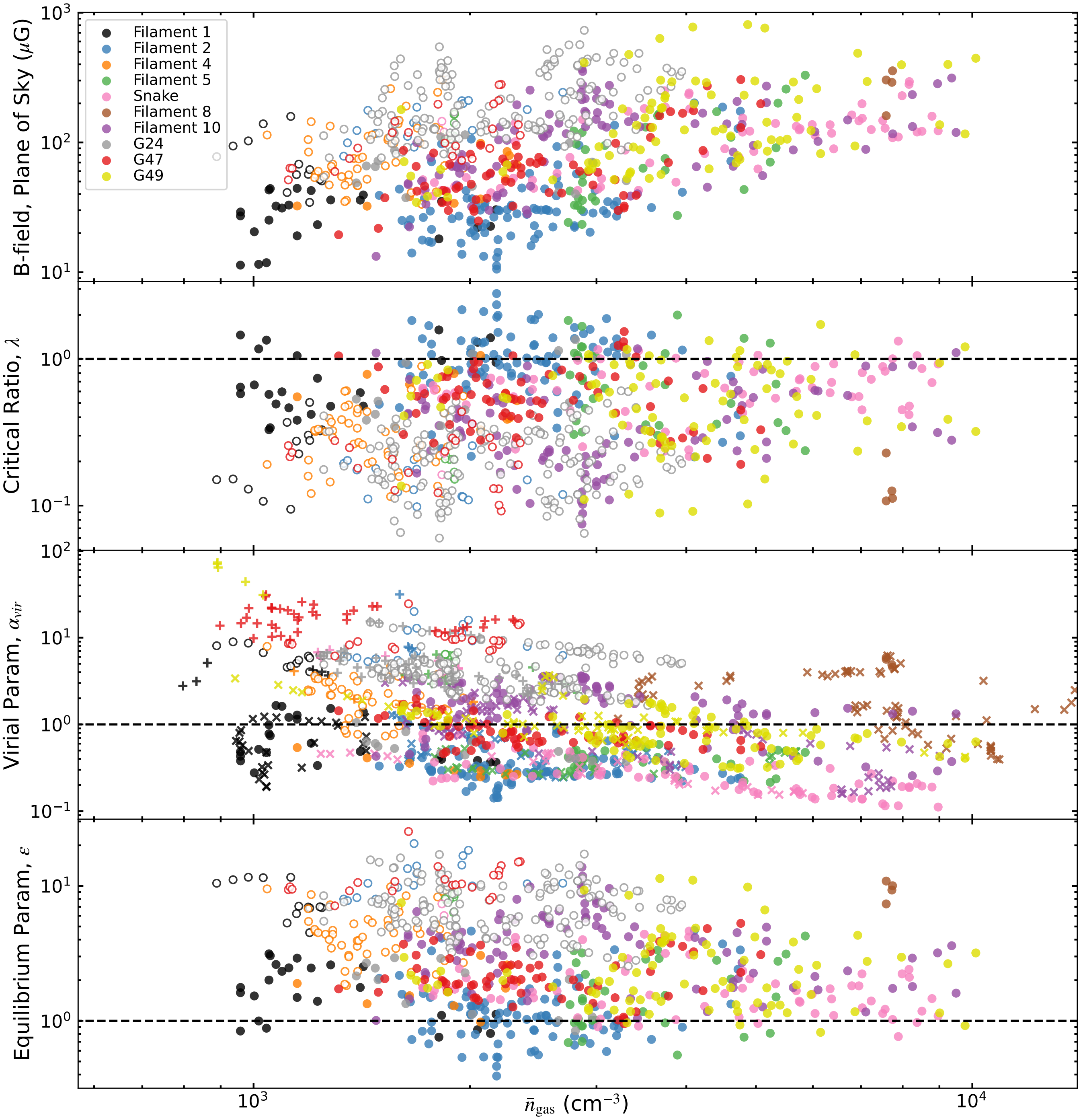

Figure 7. Values of $B_{\rm pos}$, λ, $\alpha_{\rm vir}$, and ϵ for the sliding box analysis plotted against their respective gas density, $n_{\rm gas}$, color coded for each bone. Filled and open circles show where the velocity dispersion was estimated by high- and low-density tracers, respectively. $\alpha_{\rm vir}$ is shown as filled/open circles only where there is also a $B_{\rm pos}$ estimate, and as × or + symbols where there is no $B_{\rm pos}$ estimate, yet some SOFIA data still exists in the sliding box. The × and + symbols are for $\alpha_{\rm vir}$ parameters measured with high- and low-density tracers, respectively. Dashed lines in the bottom three panels are at $y = 1$. Bones are typically magnetically subcritical (fields are dominant), but have virial parameters that are above 1, implying gravity along much of the bones may be insufficient for collapse.

The substantially large virial parameters traced by the low-density tracers may suggest that parts of the bones are not gravitationally bound. Large virial parameters have also been observed in the majority of giant molecular clouds, both in the Milky Way and in other galaxies (C. L. Dobbs et al. 2011; N. J. I. Evans et al. 2021). Y. Contreras et al. (2017) calculated the virial parameter for intermediate and high-mass clumps (parsec scale) probed by MALT90 (J. M. Jackson et al. 2013) in the Galaxy, and found that approximately 30% of them are unbound (virial parameters of 2 or more). P. C. Myers et al. (2025) also analyzed the high virial parameters toward star-forming clouds and suggested that clouds do not globally collapse, but rather locally collapse. In the simulation by A. Duarte-Cabral & C. L. Dobbs (2017), they analyzed the time evolution of giant filaments and found that they are not globally gravitationally bound, yet they may be confined by external pressure. C. Zucker et al. (2019) found that bones can form in both the arm and interarm regions through Galactic

Table 7
YSO Nearby Median Sliding Box Parameters

Bone Name	Class I+II					Class I					Class II				
	YSO Count	$B_{\rm pos}$ (μG)	λ	$\alpha_{\rm vir}$	ϵ	YSO Count	$B_{\rm pos}$ (μG)	λ	$\alpha_{\rm vir}$	ϵ	YSO Count	$B_{\rm pos}$ (μG)	λ	$\alpha_{\rm vir}$	ϵ
Filament 1	3	30	0.95	0.47	1.1	3	30	0.95	0.47	1.1	0	…	…	…	…
Filament 2	22	31	0.99	0.34	1.1	7	35	1.1	0.65	1.1	15	30	0.99	0.27	1.1
Filament 4	2	58	0.72	0.26	1.8	1	37	1.1	0.25	0.98	1	79	0.39	0.27	2.6
Filament 5	5	201	0.37	0.50	2.8	3	201	0.37	0.50	2.8	2	141	1.1	0.46	1.9
Snake	20	152	0.55	0.19	1.8	7	150	0.55	0.19	1.8	13	163	0.55	0.19	1.8
Filament 8	1	356	0.11	4.6	10	0	…	…	…	…	1	356	0.11	4.6	10
Filament 10	28	137	0.22	2.0	4.9	20	142	0.25	1.9	4.5	8	132	0.22	2.3	5.1
G24	0	…	…	…	…	0	…	…	…	…	0	…	…	…	…
G47	19	64	0.58	0.76	2.0	13	64	0.62	0.83	2.0	6	61	0.55	0.73	2.0
G49	14	152	0.44	0.63	2.4	8	235	0.63	0.61	2.1	6	152	0.43	0.88	2.7

Note. The median values in this table are not at the YSO itself, but rather the nearest spine pixel to each YSO. The table only considers YSOs within 23″ of the spine, and the sliding box analysis uses a high-density tracer and has an estimated B-field strength.

dynamics alone (i.e., ignoring feedback, local self-gravity, and B-fields). Those in spiral arms are potentially formed due to mass compressing as it enters the spiral potential, and those in the interarms are potentially formed due to differential rotation. Because of the Galactic dynamics, bones can be constantly forming and reforming. In locations where the virial parameters are high, the structure of the bones will likely persist for at least a crossing time. The velocity dispersions $\delta v_{\rm los}$ in the more diffuse areas vary but are mostly in the range of 1–4 km s^{-1}. If we approximate the bone's minimum lifetime as the crossing time, $R/\delta v_{\rm los}$, with $R \sim 1$ pc, then even diffuse parts of the bone could last for at least 0.25–1 Myr. Z18 suggest that bones typically exist for a few million years before they are destroyed by internal feedback. B-fields, along with external pressure from, for example, the weight of the Galaxy (gas + stars), may slow this dissipation and help guide the flow of gas. The models from J. D. Fiege & R. E. Pudritz (2000) showed that for helical B-fields, the toroidal component can help confine the gas by effectively squeezing the cloud. Given the complexity of B-fields in each bone, we certainly cannot rule out a toroidal component in some regions. Moreover, simulations by R. Hix et al. (2023) show that strong B-fields in quasi-cylindrical clouds can help confine gas in a direction perpendicular to the magnetic field, ultimately allowing gas to be retained for longer periods even with feedback. Additionally, bones are, for the most part, near the local minima in the Galaxy's spiral potential, which could cause mass to accumulate in these areas. It is possible that these bones will even accrete much more mass in the future. For additional discussion on filament accretion and fragmentation, see A. Hacar et al. (2023).

Despite the large virial parameters in diffuse areas, most of the bones have small virial parameters indicative of collapse in the absence of magnetic fields. To further assess the importance of B-fields in the bones, we calculate the energy density of B-fields and nonthermal kinetic energy (e.g., K. Pattle et al. 2017). The magnetic energy density of a cloud is $U_B = B^2/(8\pi)$, and the total energy is $E_B = U_B V$, where V is the volume of the bone within the sliding box. V is simply the area of the box times the average path length along the line of sight (see the appendix in S22). The nonthermal kinetic energy within the box is $E_K = 1.5M(\delta v_{\rm los})^2$ (the thermal component is negligible; $\lesssim$0.1 km s^{-1}). Repeating the sliding box analysis to estimate these parameters, and only considering locations where we have a high-density tracer, we find that E_B and E_K typically have the same order of magnitude. The median value of E_B/E_K for each bone varies from ∼1 to 5, with 2.5 being the most typical. If we take into account locations traced by the low-density tracer, the results are similar, with 2.3 being the most typical. Given the large uncertainties, especially since E_B depends on B^2, and the overall simplicity of this energy analysis, we do not interpret the results in more detail. Nevertheless, it shows that B-fields need to be considered in both the collapse and dissipation of these bones.

Despite the strong B-fields, there are young YSOs identified in the bones, which indicates that B-fields certainly have not stopped collapse altogether. In fact, we find no correlation between the YSO location and the collapse likelihood of the bone. Our estimates reflect what will happen in the future and are not indicative of the past. Moreover, a region that is magnetically subcritical can still accrete along field lines to become supercritical, allowing local collapse in the future (e.g., C. F. McKee & E. C. Ostriker 2007). Furthermore, it is possible that within our boxes, there exist high-density pockets that will collapse (or have collapsed already) to form stars. The sliding boxes used are ∼1 pc in size, which is much larger than the YSO's core size of ∼0.1 pc, and thus criticality for collapse may happen at a smaller scale. Moreover, these high-density pockets may have formed before or even simultaneously with the accumulation of mass in the bone, and the bone may serve as a reservoir for additional mass accretion.

In some bones, such as Filament 2, the cylindrical virial parameter at some locations is significantly less than unity. In simple models, this property implies a filament in global radial collapse. However, such a collapse is inconsistent with observed line profiles, with the clumpy structure of their column density, and with their relatively low star formation efficiency, typically a few percent (M. Zhang et al. 2019). Instead, these properties resemble those in turbulent MHD simulations of molecular clouds, which evolve from an initial virial parameter of ∼2 as their turbulence is allowed to dissipate on a cloud-crossing timescale. Simulations by M. Y. Grudić et al. (2019), along with STARFORGE simulations by M. Y. Grudić et al. (2021, 2022), suggest a hierarchical disordered collapse, and clouds have relatively little global collapse motion. Instead, their local motions form filaments, cores, and protostars for several Myr, with virial parameter values close to 1, until feedback from massive stars disperses most of the cloud gas. The strong B-fields of bones may further slow collapse and dispersal. We suggest that some bones, or subregions of bones with low virial/equilibrium parameter values, may undergo the kind of regional local collapse seen in these simulations.

We can also compare the B-field strengths of bones with other studies probing B-fields at similar densities (R. M. Crutcher et al. 2010; K. Pattle et al. 2023). We find that the B-field strengths vary from tens of μG to a few hundred μG, though many have higher values, especially at higher densities. The medians shown in Figure 6 and Table 6 indicate that the B-fields are most commonly in the 30–150 μG range. The median strengths are likely closer to the lower range of these values since B-fields are probably weaker in regions where we were unable to make estimates with the sliding box. The bones, at the scales probed in the sliding box analysis, have typical densities of $10^3\,\mathrm{cm}^{-3}$–$10^4\,\mathrm{cm}^{-3}$. As a comparison, H I and OH Zeeman observations (R. M. Crutcher et al. 2010, and references therein), which measure the line-of-sight B-field, B_{los}, have shown that at these densities, B-fields are typically only $\sim$10 μG, with maximum values around 100 μG. However, K. Pattle et al. (2023) collected DCF estimates from the literature and found B-field strengths quite consistent with what we observe in the bones, with some values reaching over 1 mG at $\sim 10^4\,\mathrm{cm}^{-3}$. K. Pattle et al. (2023) and references therein discuss the discrepancy between Zeeman B_{los} measurements and the DCF B_{pos} estimates, but said there is no clear resolution to this discrepancy. It is worth noting that the polarization morphology toward the bones (Figure 1 and Appendix A) often changes rapidly in the plane of the sky, so it would be reasonable to believe that fields also change directions frequently within the large beam (usually $>1'$) used in the Zeeman observations, lowering the Zeeman signals compared to the unidirectional B-field case.

R. M. Crutcher et al. (2010) and K. Pattle et al. (2023) show a relation between B and n_{gas}, and the relation is also apparent in Figure 7, albeit with significant scatter. However, the relations observed by R. M. Crutcher et al. (2010) and K. Pattle et al. (2023) span many orders of magnitude, whereas we are analyzing the relationship over just a single order of magnitude. Within this narrower range, the dispersion of B-field strengths with density appears to be similar to the above studies.

B. Zhao et al. (2024) produced galactic MHD zoom-in simulations with supernova feedback, finding that fields can be made more orderly and strengthened due to expanding shells. They found that fields are both parallel and perpendicular to filaments. In our study, four bones exhibited little perpendicular alignment at high column densities: G24, G49, Filament 8, and Filament 10 (Section 3.1). Filament 8 and Filament 10 even showed a preference for parallel alignment. Additionally, three bones had virial parameters greater than 1 throughout their entire length, indicating that these bones are not globally collapsing at parsec scales: G24, Filament 8, and Filament 10 (Figure 7). This suggests that bones without perpendicularly aligned B-fields generally coincide with those having high virial parameters. G49 is an exception, as it contains many regions where the virial parameter is below 1. Therefore, while there is some evidence that perpendicular B-fields may indicate bones more likely to collapse, the current sample size is not large enough to provide strong statistical support for this conclusion. Whether known Galactic shells impact such alignment, as seen in the B. Zhao et al. (2024) simulations, is left for future work.

The lack of global alignment, either parallel or perpendicular, throughout the entirety of most bones may indicate that B-fields were not the dominant force in their formation. For example, galactic forces such as galactic potential of spiral arms and/or differential rotation might be their origins (C. Zucker et al. 2019). Nevertheless, the present-day B-fields are strong and frequently very structured on a local clump (few parsec) scales. If B-fields were also strong during the formation of the bones, the present-day disordered B-fields may indicate that bones originally formed as a strand of clumps within a gravitational potential well. If that is the case, cylindrical geometry for the entire bone filaments may be a poor assumption if the clumps do not coalesce. On the contrary, it is also possible that a variety of feedback mechanisms, both within and outside of the bones, have changed fields from originally aligned to less aligned.

Finally, the analysis in this paper has a selection bias of long structures that are parallel to the Galactic plane. Whether similar analyses of other Galactic structures would yield the same results remains unclear.

6. Summary

In this paper, we analyze the inferred magnetic field morphology for all 10 bones in the FIELDMAPS survey, using a method similar to that applied to G47 in S22. The images reveal that the B-fields are structured, but morphologically diverse across the bones. We first examine the alignment of magnetic fields with the spines of the bones, as well as the locations of high column density and YSOs. We find the following:

1. Along each bone, there is no dominant preferred orientation (e.g., parallel or perpendicular) between the spine and the B-fields. However, all bones except Filament 8 and Filament 10 show a slight preference for perpendicular alignment between the spine and the B-fields. Filament 8 and Filament 10, on the other hand, display a slight preference for parallel alignment.
2. At lower column densities ($N_{\mathrm{gas}} \sim 0.5$–$1 \times 10^{22}\,\mathrm{cm}^{-2}$), B-field alignment with the bone is random. This is consistent with Planck Collaboration et al. (2016), as these column densities represent where they saw the alignment of B-fields transition from mostly parallel with the elongations to not parallel. For bones showing a preference for perpendicular alignment, this tendency generally becomes more pronounced at higher column densities. In contrast, the only two bones observed in Quadrant 4 of the Galaxy, Filament 8 and Filament 10, exhibit a greater degree of parallel alignment at higher column densities.
3. Class I and Class II YSOs are usually found at locations of higher column densities. Class I YSOs are more likely at locations of higher column density than Class II YSOs, indicating YSOs either migrate or the bone evolves significantly during their evolution. However, they are not significantly more likely to form at places with perpendicular or parallel alignment. Assuming the YSO migration rate and dissipation rate are small, the lack of alignment suggests that YSOs form at high column

densities, but are ignorant of the direction of the local magnetic fields' direction or their potential guiding of gas flow on the ∼0.1–1 pc scales probed by our observations.

Next, we slide a box of approximately 1 pc in size down the spine of each bone, allowing it to rotate along the direction of the spine. Within the box, we estimate the average B-field and investigate its importance relative to gravity. We find the following:

1. The median B-field strengths differ by up to a factor of a few between the bones, yet B-fields can vary significantly across bones. Nevertheless, the parsec-scale B-field strengths for the bones are typically 30–150 μG. There exists a slightly positive correlation between density and B-field strengths.
2. We compare the calculated mass-to-flux ratio with the mass-to-flux ratio needed for gravitational collapse using the critical ratio, λ. We find that λ values are usually much less than 1. The low values of λ indicate that even if we are overestimating the B-field strengths, B-fields likely provide at least some support against gravitational collapse in the bones.
3. The cylindrical virial parameter $\alpha_{\rm vir}$ is frequently found to be less than 1, suggesting that the bones would likely collapse in the absence of magnetic fields. The low-density tracers indicate high virial parameters at some locations of the bones, suggesting gravitationally bound bones may be embedded in unbound gas. Given that λ is generally low everywhere and the magnetic energy density is high, B-fields may be important for both the collapse and dissipation of mass from the bones.
4. Few locations across any of the bones show low $\alpha_{\rm vir}$ and high λ, which we quantify with the equilibrium parameter, ϵ. Given the uncertainties in the estimates, some bones may still have locations likely to collapse. Filament 2 appears to be the most likely bone to form additional stars now or in the near future.

We suggest that bones may form via mass collecting in the spiral potential. Magnetic fields are significant and may help aid the lifetime of the bones by slowing down collapse and dissipation. Given that there are many known YSOs across the bones, yet much of the bones appear not to be critical to collapse, parts of the bones may have been denser in the past, or dense pockets at smaller scales (e.g., cores) can collapse to form more YSOs. Moreover, YSOs may have resulted from high-density cores that formed either concurrently with or even before the bones.

Acknowledgments

We thank an anonymous referee for critical comments that greatly improved the paper. This paper is based on observations made with the NASA/DLR SOFIA. SOFIA was jointly operated by the Universities Space Research Association, Inc. (USRA), under NASA contract NNA17BF53C, and the Deutsches SOFIA Institut (DSI) under DLR contract 50 OK 0901 to the University of Stuttgart. Financial support for this work was provided by NASA through award Nos. 05_0109 and 08_0186 issued by USRA. The Green Bank Observatory is a facility of the National Science Foundation operated under cooperative agreement by Associated Universities, Inc. This publication is based on data acquired with the Atacama Pathfinder Experiment (APEX) under programs 092.F-9315 and 193.C-0584. APEX is a collaboration among the Max Planck Institute for Radio Astronomy, the European Southern Observatory, and the Onsala Space Observatory. The processed data products are available from the SEDIGISM survey database,[23] which was constructed by James Urquhart and hosted by the Max Planck Institute for Radio Astronomy. We thank James Urquhart for early help with the data products. L. W.L. acknowledges support from NSF AST-1910364 and NSF AST-2307844. T.G.S.P. gratefully acknowledges support by the National Science Foundation under grant No. AST-2009842 and AST-2108989, and by NASA award No. 09-0215 issued by USRA. We thank Michael Gordon for his effort in setting up the on-the-fly maps for the FIELDMAPS project and Sachin Shenoy for helping us with the SOFIA pipeline for data reduction. We thank Leah Zuckerman for her early efforts in analyzing the FIELDMAPS data.

Facilities: SOFIA (HAWC+), Herschel, APEX, GBT, FCRAO.

Software: `APLpy` (T. Robitaille & E. Bressert 2012), `astropy` (Astropy Collaboration et al. 2013, 2018), `MAGNETAR` (J. D. Soler et al. 2013), `Reproject` (T. Robitaille et al. 2020).

Appendix A
Images of the Magnetic Field Morphology for All Bones

Figures 8–18 present the vector and LIC maps for all bones, as only Filament 1 is shown in the main text (Figure 1). Spacing for the top panels is shown for every 2 pixels, which is approximately Nyquist sampling. We choose to display vectors this way, as it shows the most robust detail possible of the magnetic field morphology. Some readers may prefer more spacing between vectors for some bones to make the morphology clearer. Those sorts of maps are shown in C25.

---

[23] https://sedigism.mpifr-bonn.mpg.de/index.html

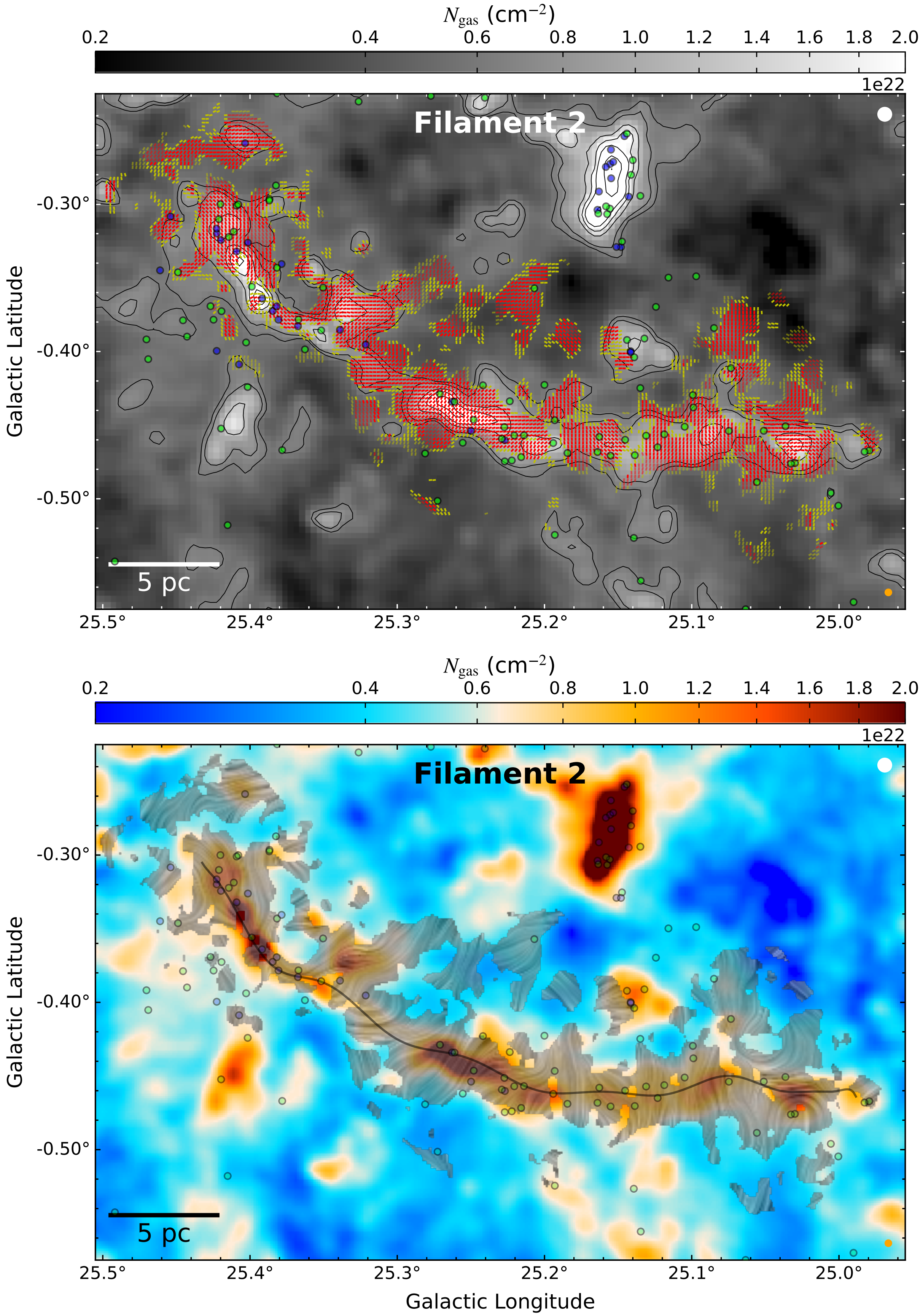

Figure 8. Figure caption is the same as that of Figure 1, except now for Filament 2.

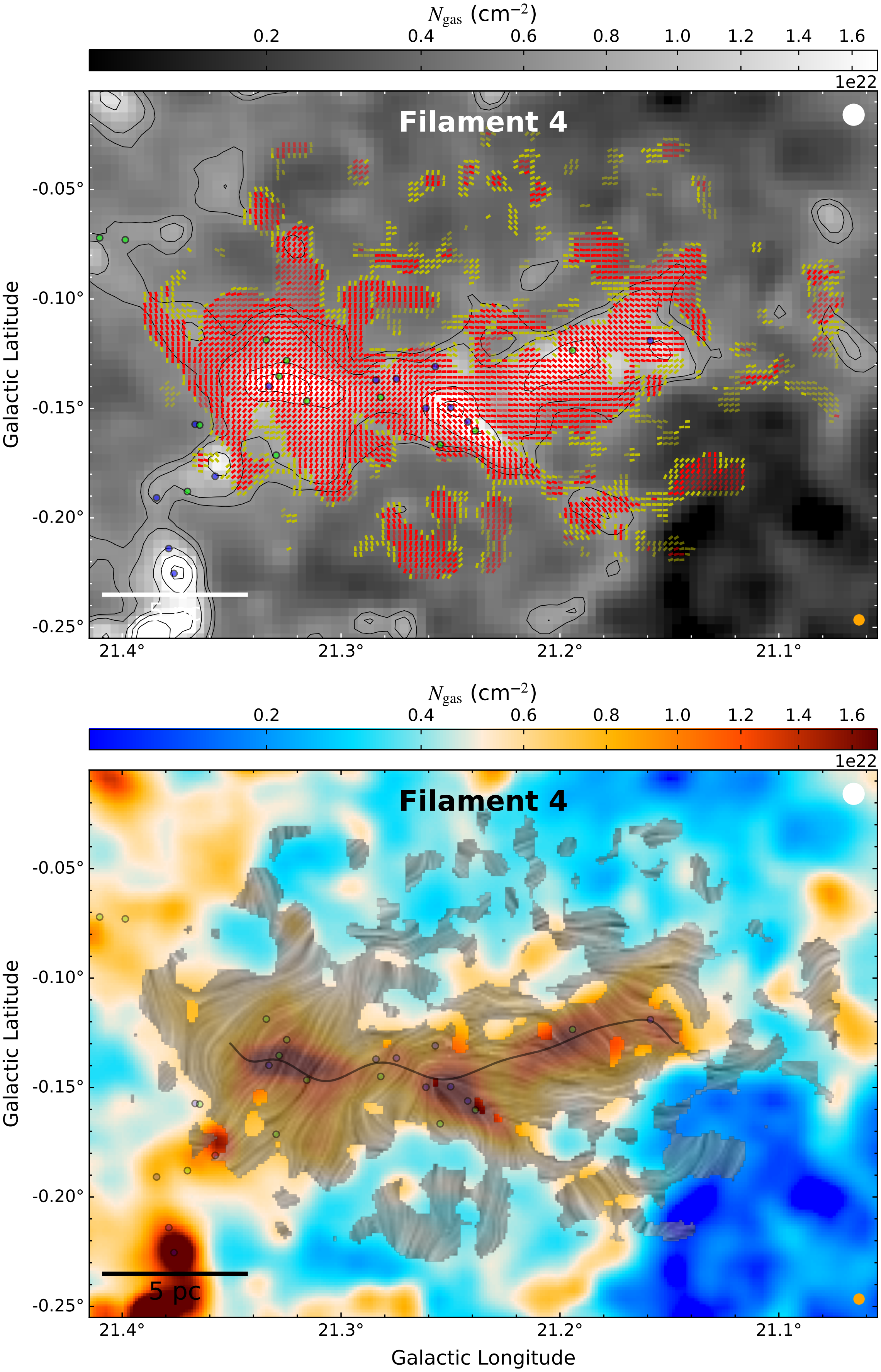

Figure 9. Figure caption is the same as that of Figure 1, except now for Filament 4.

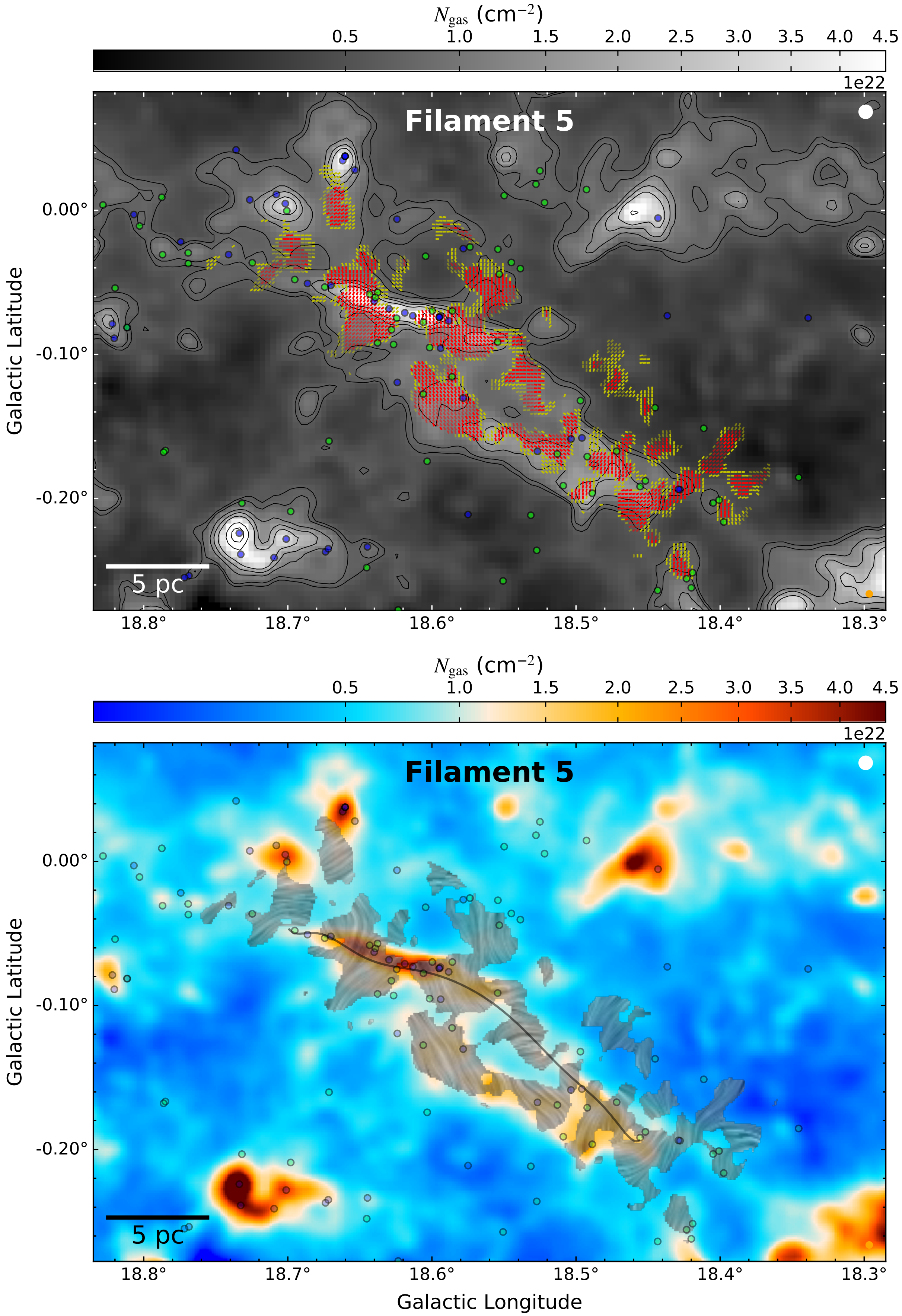

Figure 10. Figure caption is the same as that of Figure 1, except now for Filament 5.

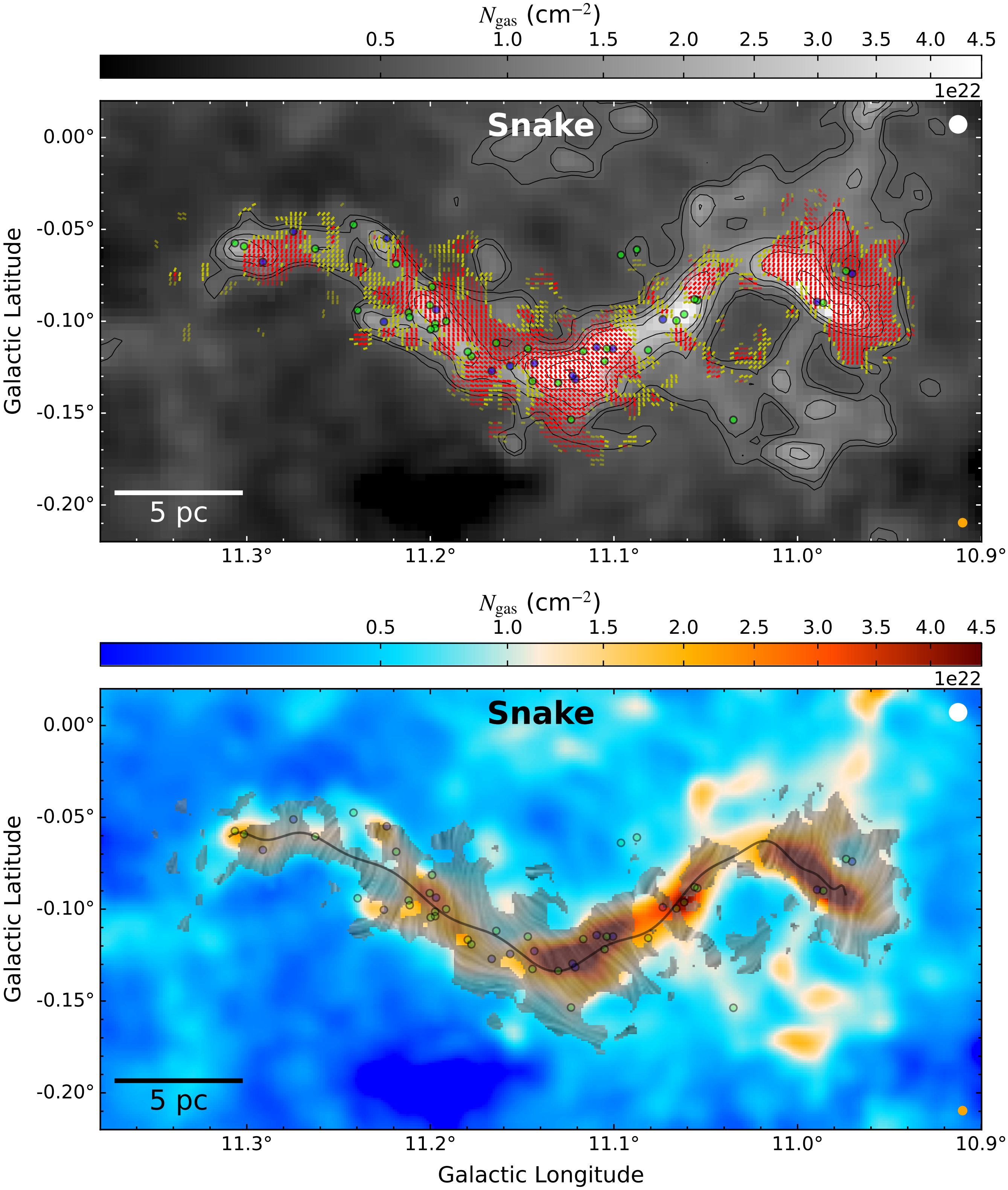

Figure 11. Figure caption is the same as that of Figure 1, except now for the Snake.

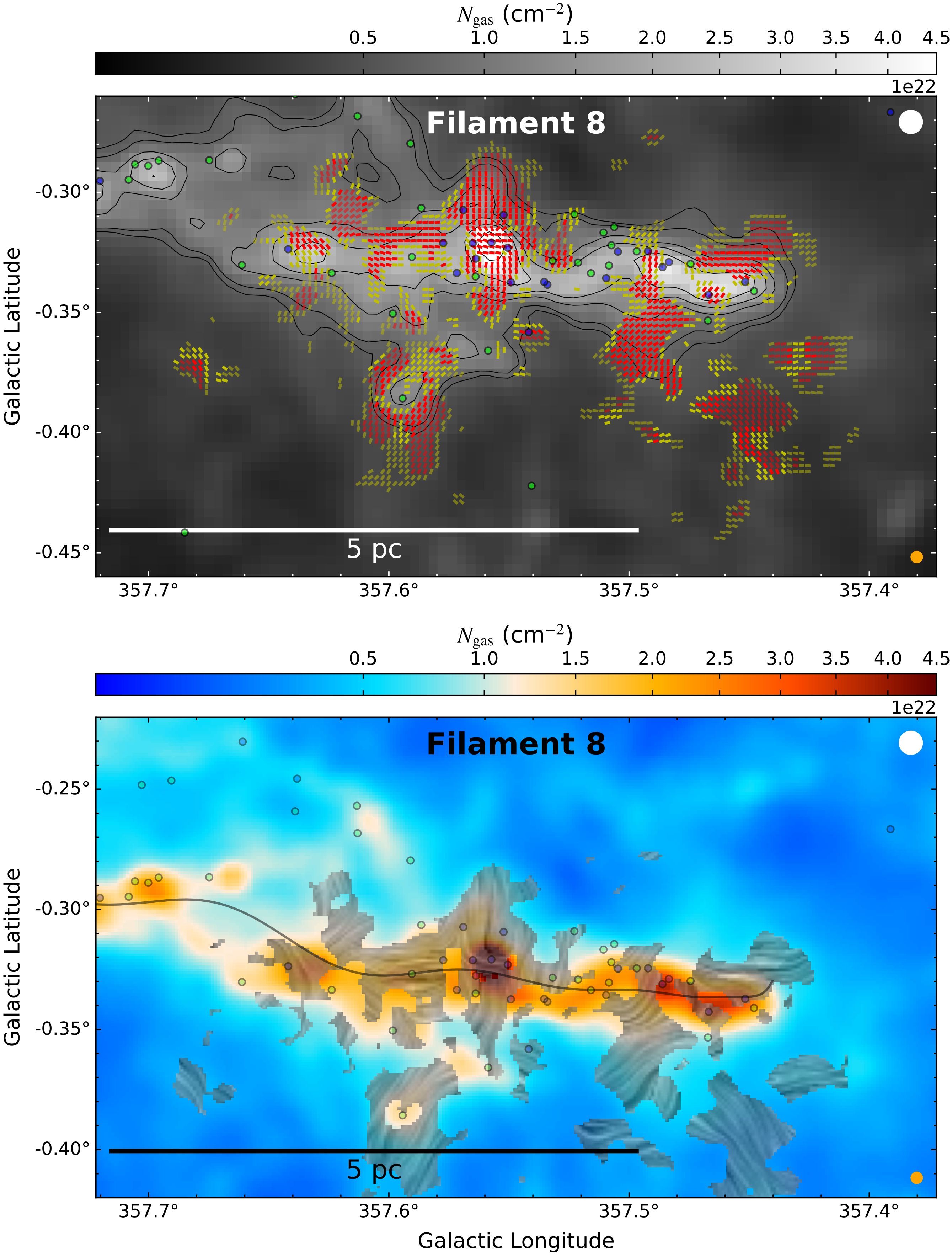

Figure 12. Figure caption is the same as that of Figure 1, except now for Filament 8.

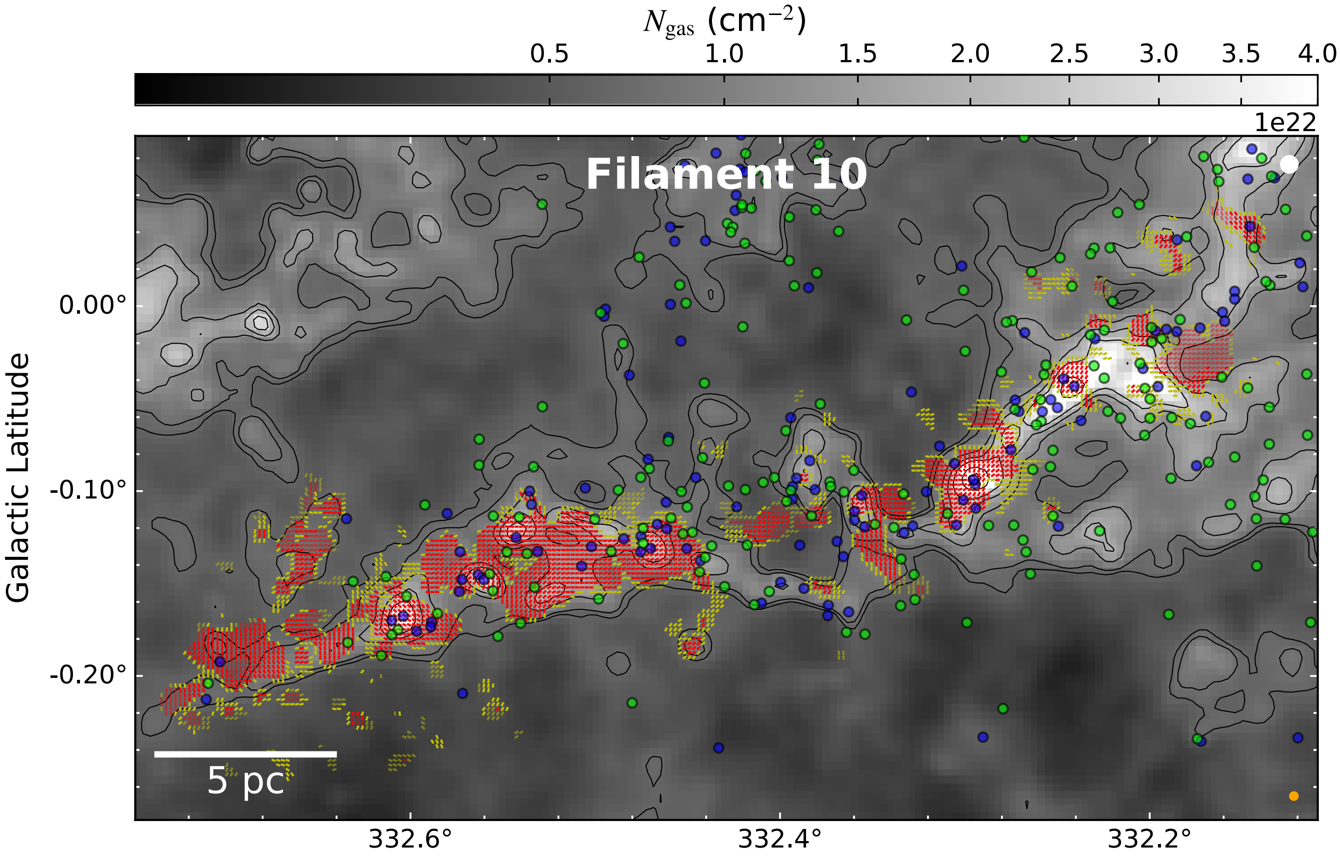

Figure 13. Figure caption is the same as that in the top panel of Figure 1, except now for Filament 10.

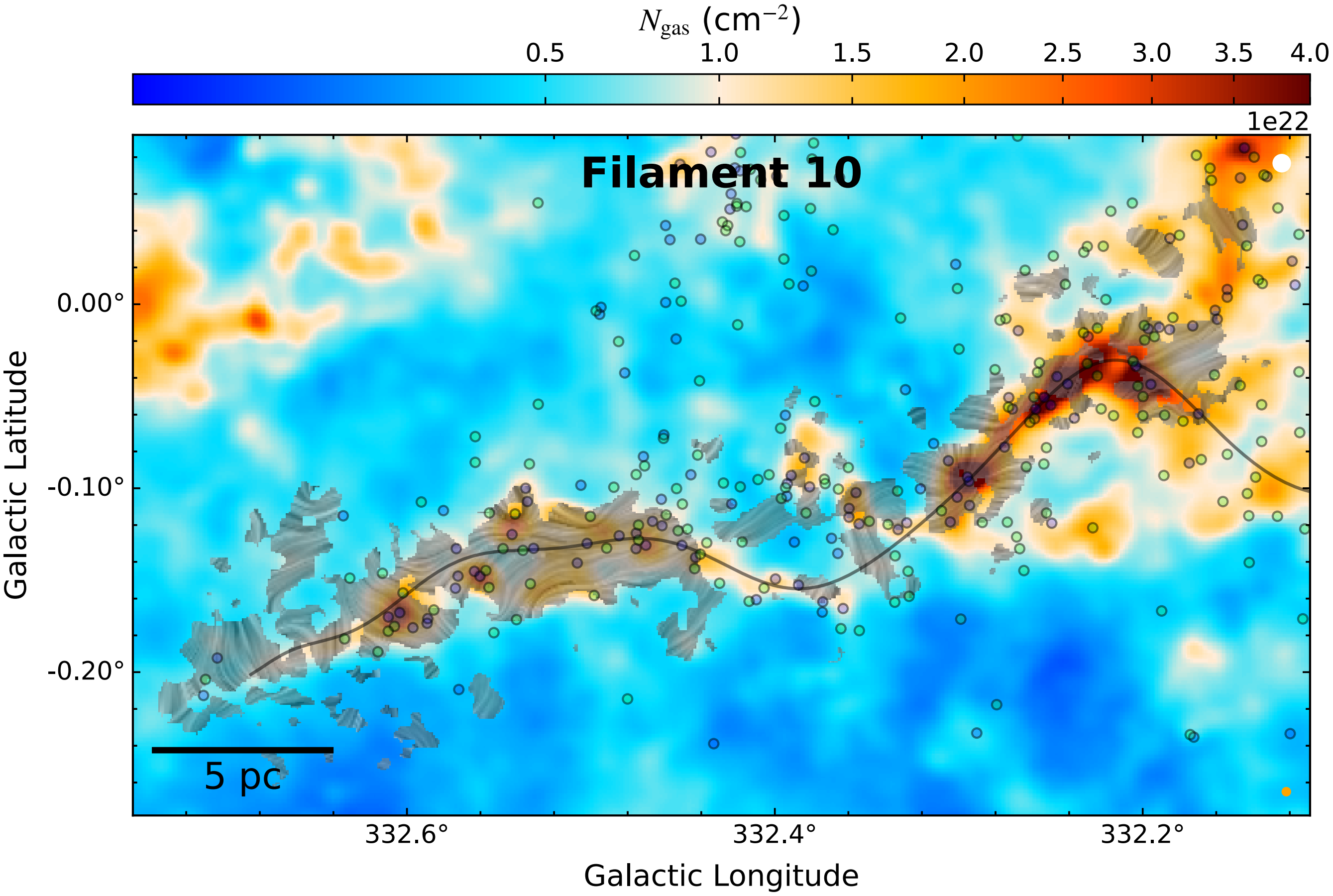

Figure 14. Figure caption is the same as that in the bottom panel of Figure 1, except now for Filament 10.

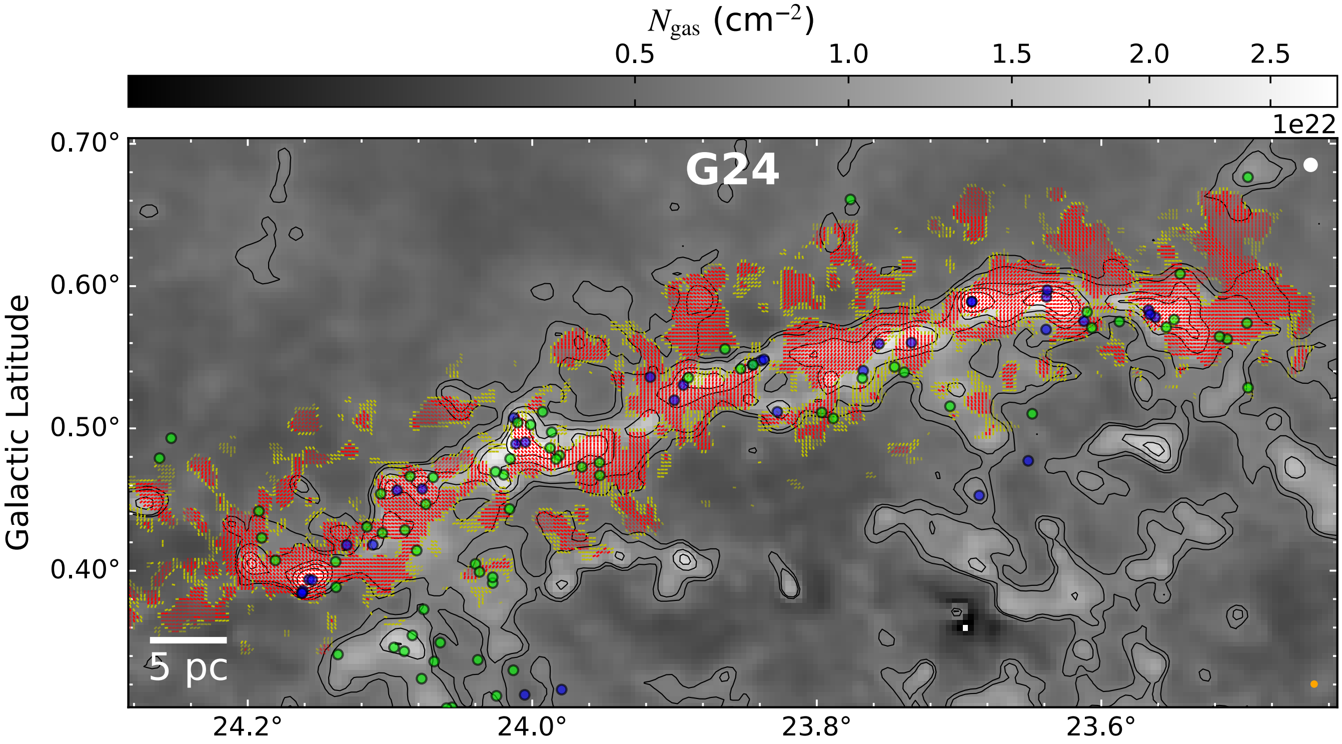

Figure 15. Figure caption is the same as that in the top panel of Figure 1, except now for G24.

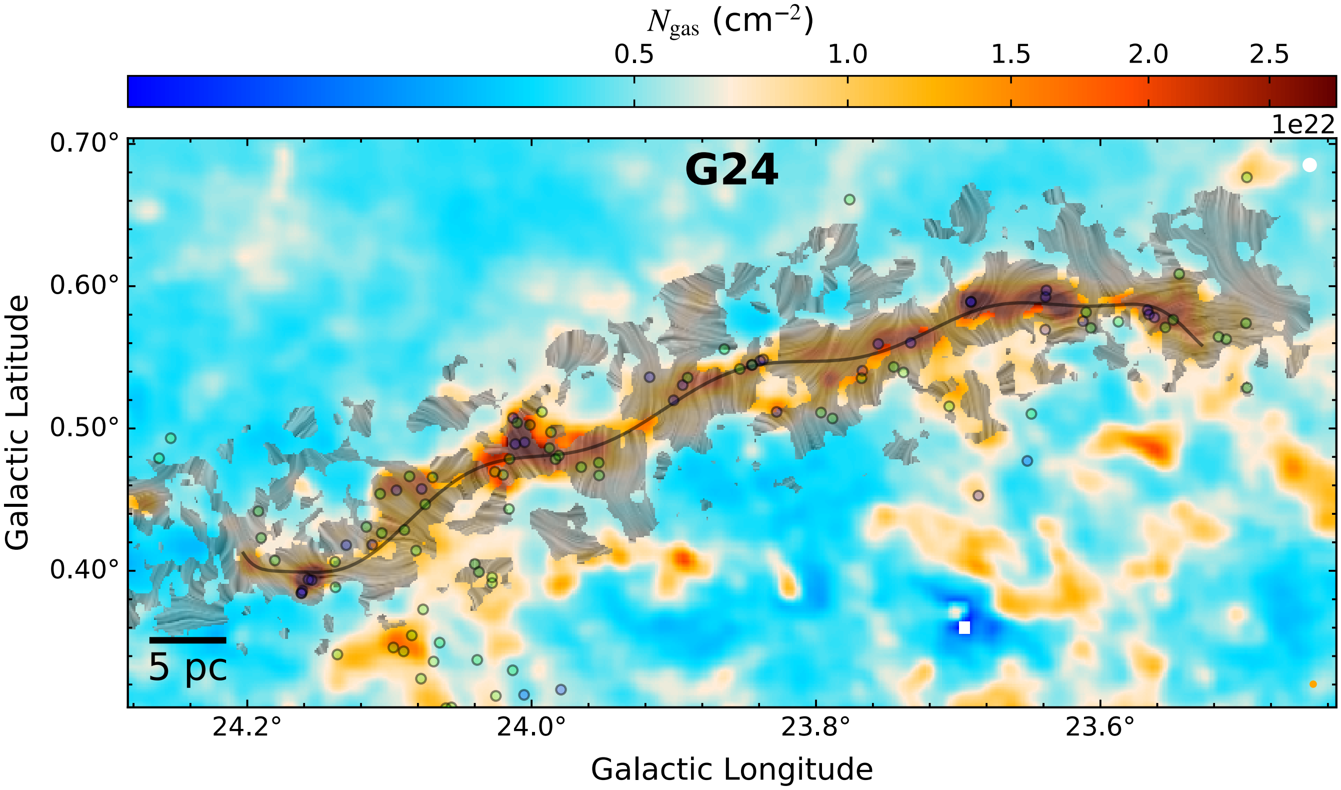

Figure 16. Figure caption is the same as that in the bottom panel of Figure 1, except now for G24.

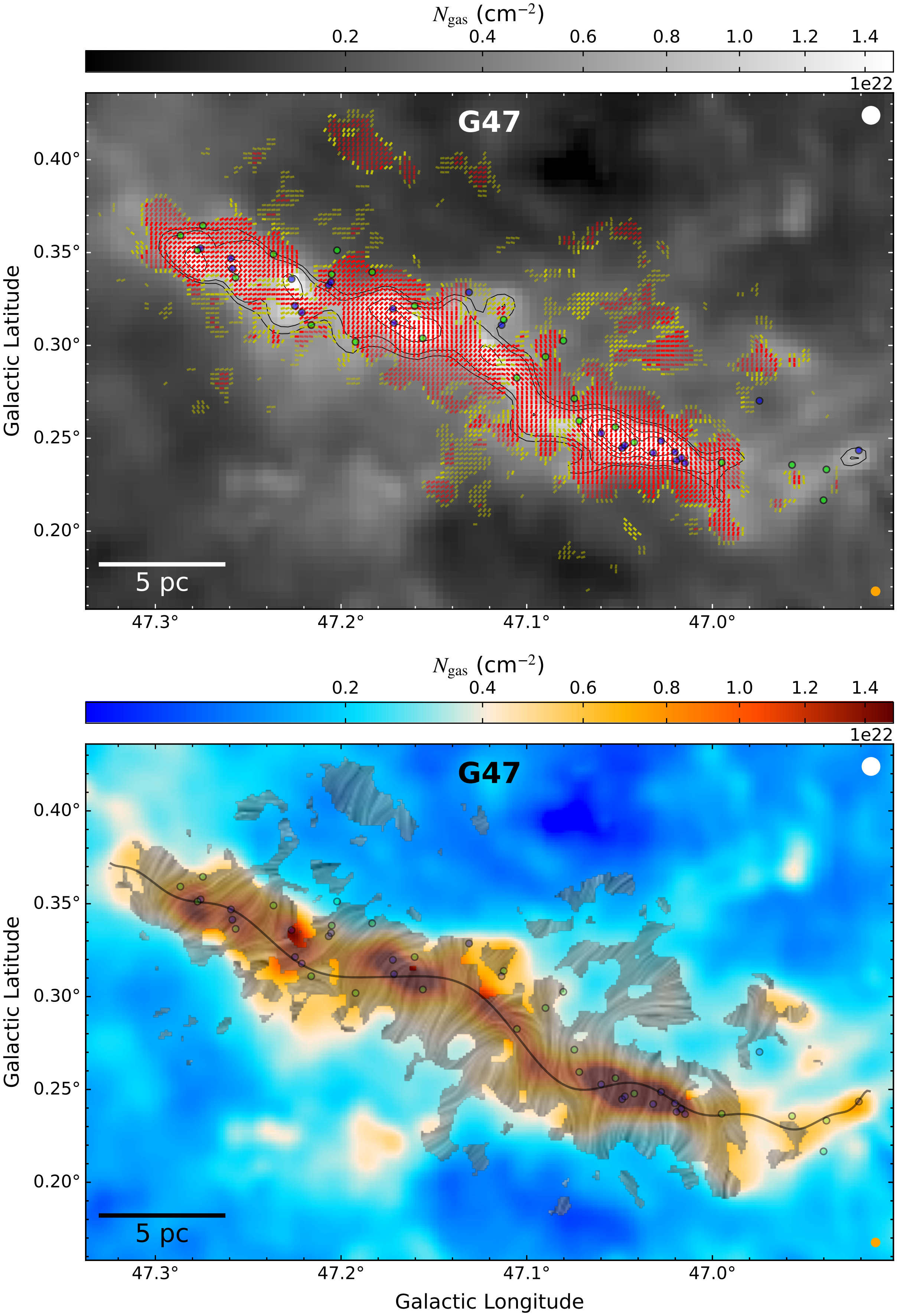

Figure 17. Figure caption is the same as that of Figure 1, except now for G47.

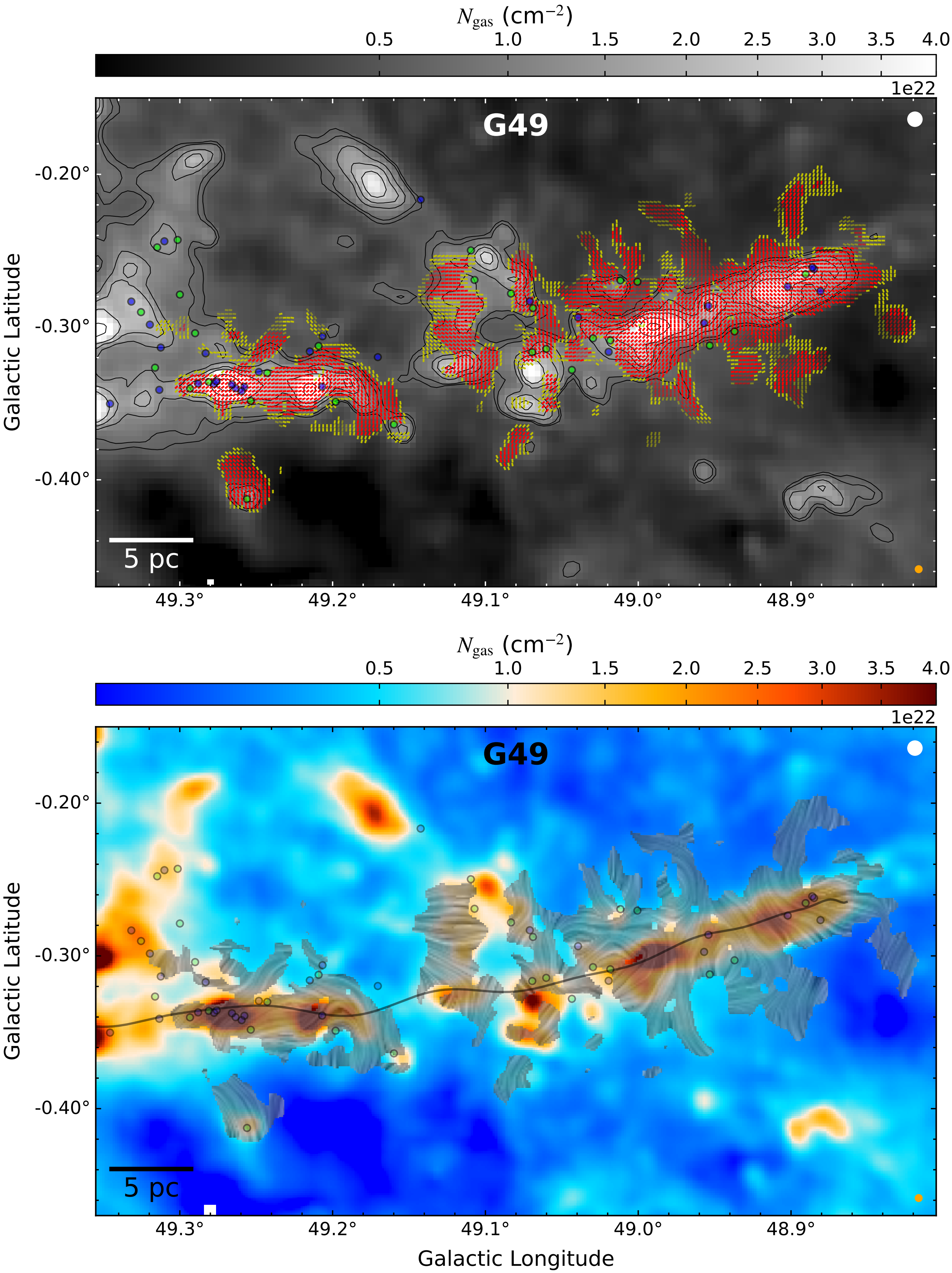

Figure 18. Figure caption is the same as that of Figure 1, except now for G49.

Appendix B
Velocity Dispersion Comparisons

In Table 2, we report the low- and high-density line tracers used for the paper. In summary, all bones use $NH_3(1,1)$ for their high-density tracer, except Filament 8 and Filament 10, which use $C^{18}O(2–1)$. For low-density tracers, all bones use $^{13}CO(1–0)$, except the Snake, Filament 8, and Filament 10, which use $^{13}CO(2–1)$. For the sliding box analysis (Section 4), we are specifically interested in measuring the line-of-sight velocity dispersion $\delta v_{\rm los}$. Here, we do a point-by-point comparison of the velocity dispersions measured near the spine of the bone by choosing only those pixels within 23″ of the polynomial fit of the spine of the bone (see Section 2.3), and where we detect polarization at a level of $P_{\rm frac}/\sigma_{P_{\rm frac}} > 2$. Figure 19 shows the ratio in velocity dispersions of the high-density tracer ($\delta v_{\rm los,ld}$) and low-density tracer ($\delta v_{\rm los,hd}$) as a function of column density. Points in the plot are heavily oversampled, as the values use the velocity dispersion maps that have been regridded to the SOFIA resolution since the regridded maps are used for the sliding box analysis. Since median values are reported, they are largely unaffected by the oversampling.

$\delta v_{\rm los,ld}$ is consistently higher than $\delta v_{\rm los,hd}$, usually by a factor of ∼2 or more, and the median values are mostly consistent with column density. The obvious exception is Filament 10, and the higher column density data for Filament 8. These two bones use different line tracers from the SEDIGISM data, which is different than the rest of the sample. These values may be expected to be closer, as the tracers are taken at the same angular resolution (30″), while the $NH_3(1,1)$ and $^{13}CO(1–0)$ are at different resolutions (32″ versus 45″), and the higher-*J* transitions trace higher densities. However, we caution that $C^{18}O(2–1)$, which is used for Filament 8 and Filament 10, may not be as good as a high-density tracer as $NH_3(1,1)$; the velocity dispersions ratios for the Snake, which

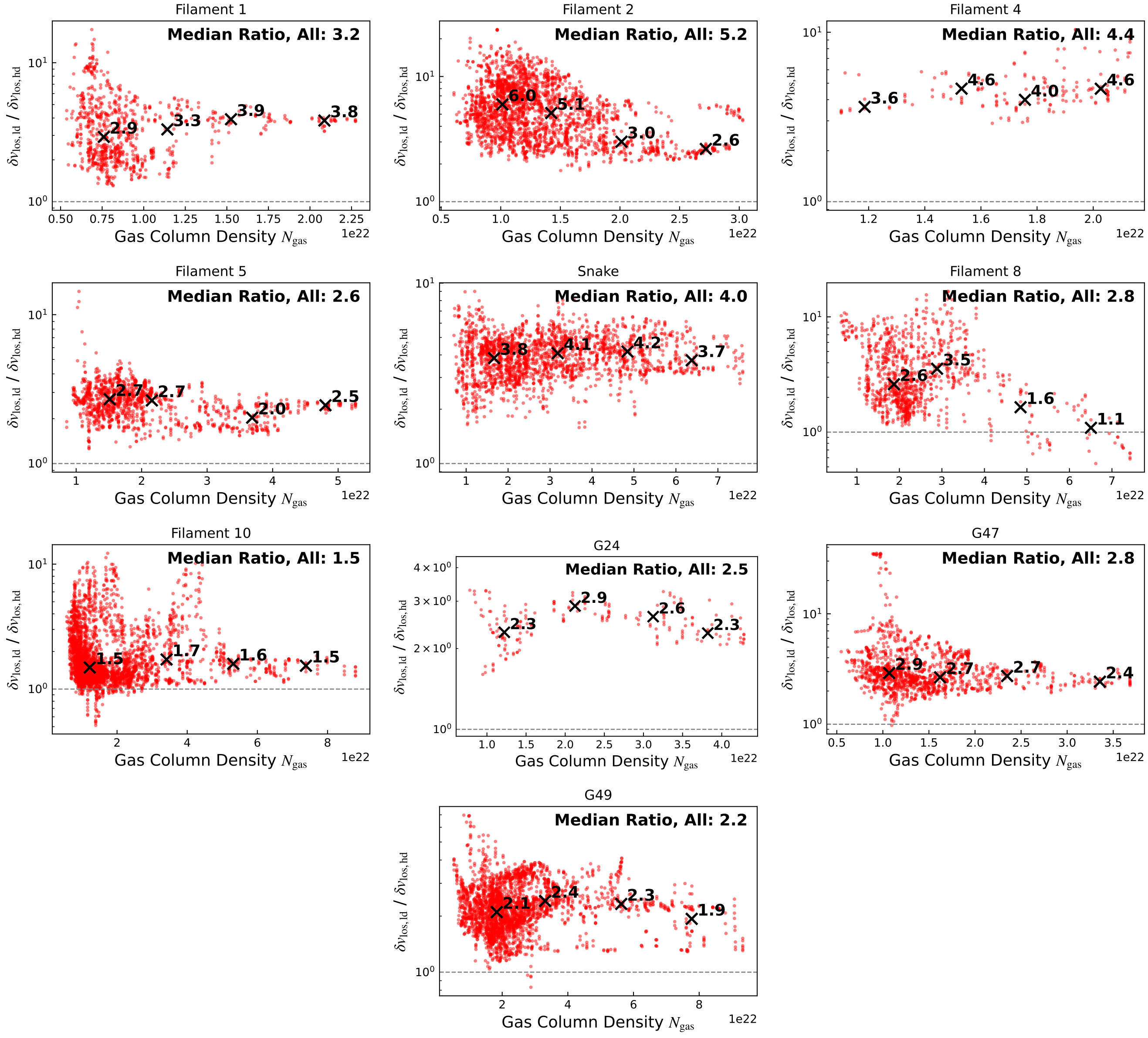

Figure 19. Ratio in measured velocity dispersions of the high-density tracer ($\delta v_{\rm los,ld}$) and low-density tracer ($\delta v_{\rm los,hd}$) as a function of gas column density $N_{\rm gas}$ for each bone. Data are binned in four equal-width intervals in $N_{\rm gas,}$ with black crosses showing the median ratio per bin. The dashed line marks a ratio of unity. The overall median ratio is indicated in the upper right of each panel. Comparisons are only shown where $P_{\rm frac}/\sigma_{P_{\rm frac}} > 2$ and pixels are no more than 23″ from the spine.

compares $NH_3(1,1)$ to $^{13}CO(2–1)$, are higher than that of these two bones, indicating that $NH_3(1,1)$ spectra likely have smaller velocity dispersions. The fact that $C^{18}O(2–1)$ may overestimate the velocity dispersion is reflected in Figure 7, as Filament 8 and Filament 10 tend to show higher virial parameters than the other bones.

The velocity dispersion ratios are exceptionally high for Filament 2. Visual inspection of the spectra across the bone show that $^{13}CO(1–0)$ has a severely flattened peak, which is a result of a very optically thick line. In turn, fitting spectra to such optically thick lines results in large velocity dispersions.

Appendix C
CDFs of Alignment

This appendix provides additional figures of CDFs presented in Section 3, which compare the distribution of the projection angle difference between the bone's spine and the B-field position angle for each pixel. Figures 20 through 23 separate the data presented in Figure 5 into four equal-sized quartiles based on the column density of the angle comparison.

There is no general trend that can be seen across all bones for these particular CDFs, other than that which matches the general findings seen in Figure 4, as discussed in Section 3. Notably, Filament 4, Filament 5, the Snake, and G47 spine B-field angle differences appear even more perpendicular at the highest column densities (Figure 23). G47 in particular appears quite perpendicular at the highest column densities, matching closely with the cyan line, which is the case where G47 is perfectly in the plane of the sky and the B-fields are projected at random. Filament 4 and Filament 5 show more parallel features at the lowest column densities (Figure 20) when compared to all the data (Figure 5), while G47 is similar. The Snake, on the other hand, is a bit of an oddity, as it appears more perpendicular at both lower and higher column densities, and is slightly less perpendicular in the second quartile, and has roughly random and even slightly parallel in the third quartile. Filament 10 at the highest column densities (Figure 23) spine/B-field alignment appears even more parallel, which is also evident in Figure 4.

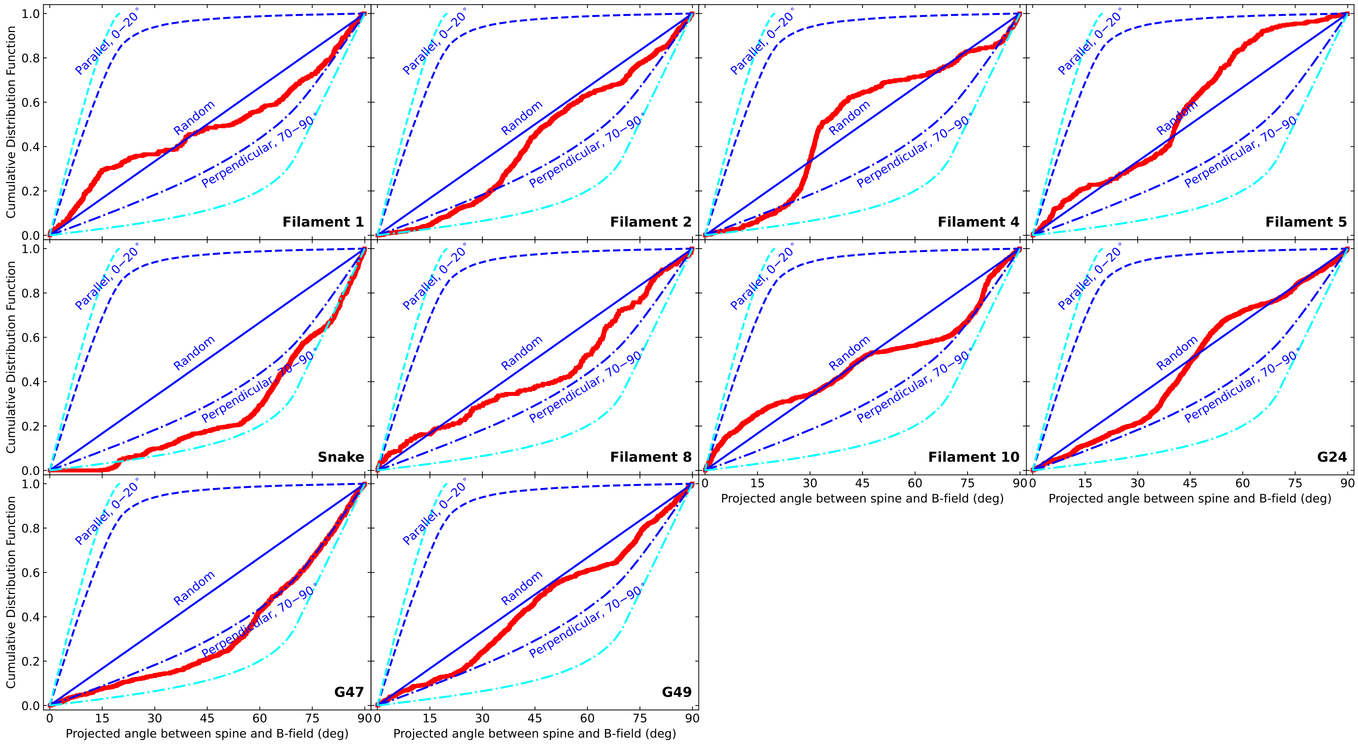

Figure 20. Caption is the same as that of Figure 5, but now only showing data in the first quartile (lowest values) for column density.

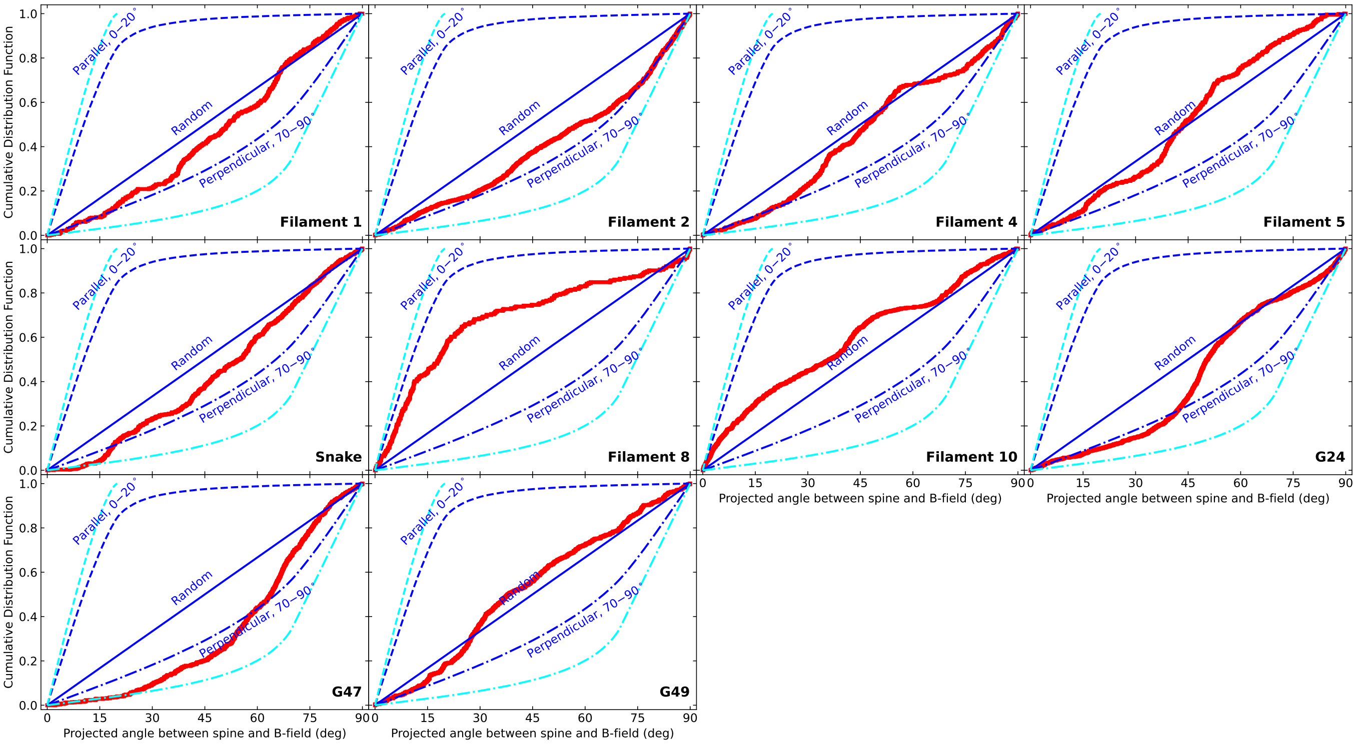

Figure 21. Caption is the same as that of Figure 5, but now only showing data in the second quartile for column density.

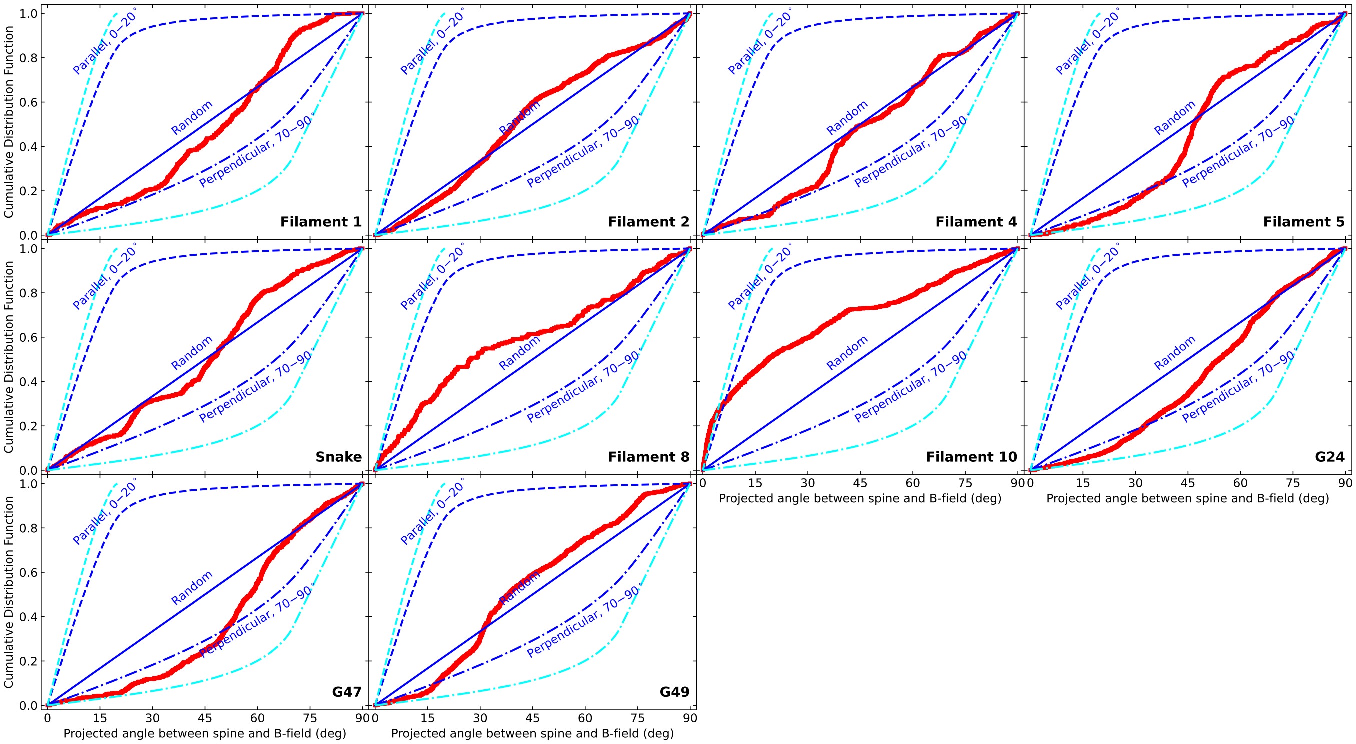

Figure 22. Caption is the same as that of Figure 5, but now only showing data in the third quartile for column density.

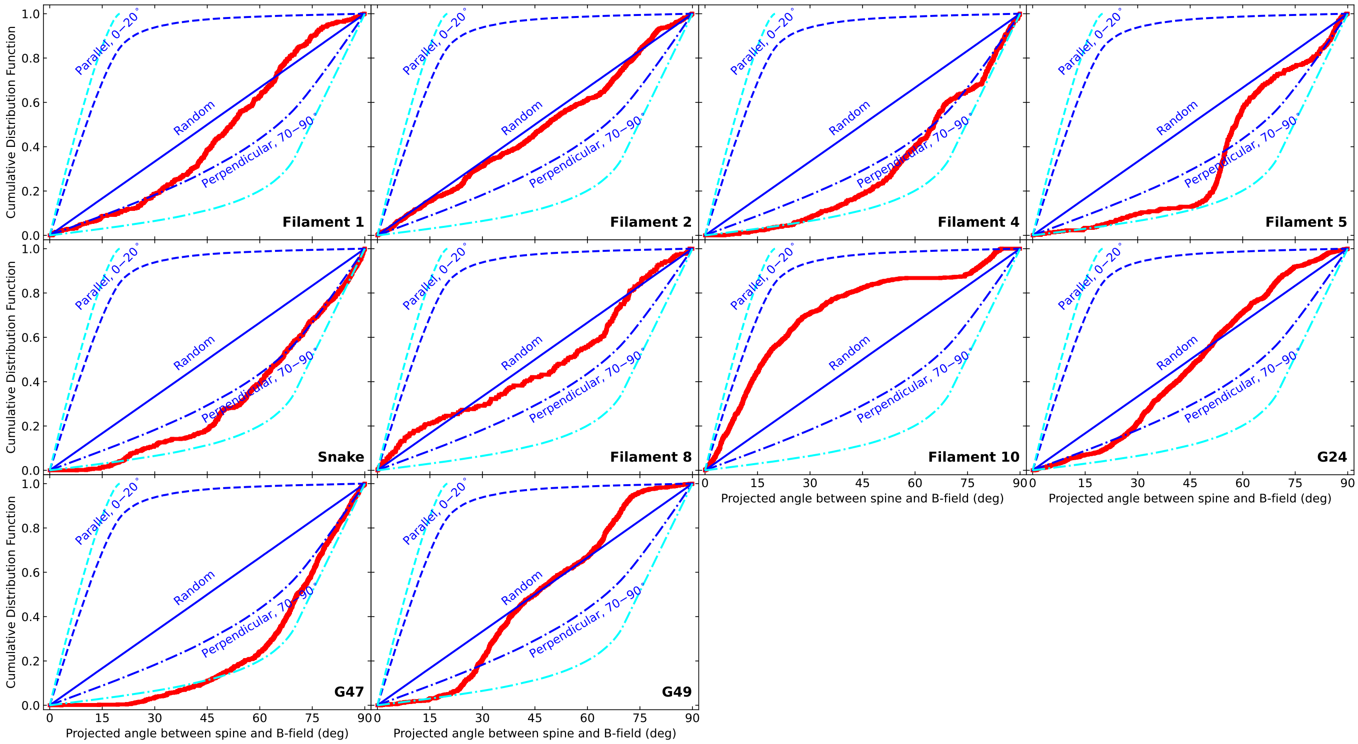

Figure 23. Caption is the same as that of Figure 5, but now only showing data in the fourth quartile (highest values) for column density.

ORCID iDs

Ian W. Stephens https://orcid.org/0000-0003-3017-4418
Simon Coudé https://orcid.org/0000-0002-0859-0805
Philip C. Myers https://orcid.org/0000-0002-2885-1806
Catherine Zucker https://orcid.org/0000-0002-2250-730X
James M. Jackson https://orcid.org/0000-0002-3466-6164
B.-G. Andersson https://orcid.org/0000-0001-6717-0686
Archana Soam https://orcid.org/0000-0002-6386-2906
Patricio Sanhueza https://orcid.org/0000-0002-7125-7685
Taylor Hogge https://orcid.org/0000-0002-7211-7078
Giles Novak https://orcid.org/0000-0003-1288-2656
Sarah Sadavoy https://orcid.org/0000-0001-7474-6874
Thushara Pillai https://orcid.org/0000-0003-2133-4862
Zhi-Yun Li https://orcid.org/0000-0002-7402-6487
Leslie W. Looney https://orcid.org/0000-0002-4540-6587
Koji Sugitani https://orcid.org/0000-0003-3081-6898
Andrés E. Guzmán https://orcid.org/0000-0003-0990-8990
Alyssa Goodman https://orcid.org/0000-0003-1312-0477
Takayoshi Kusune https://orcid.org/0000-0002-9218-9319
Miaomiao Zhang https://orcid.org/0000-0002-6388-649X
Nicole Karnath https://orcid.org/0000-0003-3682-854X

References

Andersson, B.-G., Lazarian, A., & Vaillancourt, J. E. 2015, ARA&A, 53, 501
André, P., Men'shchikov, A., Bontemps, S., et al. 2010, A&A, 518, L102
Astropy Collaboration, Price-Whelan, A. M., Sipőcz, B. M., et al. 2018, AJ, 156, 123
Astropy Collaboration, Robitaille, T. P., Tollerud, E. J., et al. 2013, A&A, 558, A33
Benjamin, R. A., Churchwell, E., Babler, B. L., et al. 2003, PASP, 115, 953
Borlaff, A. S., Lopez-Rodriguez, E., Beck, R., et al. 2021, ApJ, 921, 128
Cabral, B., & Leedom, L. C. 1993, in Proc. of the 20th Annual Conf. on Computer Graphics and Interactive Techniques (New York: ACM), 263
Carey, S. J., Noriega-Crespo, A., Mizuno, D. R., et al. 2009, PASP, 121, 76
Clemens, D. P., Cashman, L. R., Cerny, C., et al. 2020, ApJS, 249, 23
Contreras, Y., Rathborne, J. M., Guzman, A., et al. 2017, MNRAS, 466, 340
Coudé, S., Stephens, I. W., Myers, P. C., et al. 2026, ApJS, 282, 2
Crutcher, R. M., Nutter, D. J., Ward-Thompson, D., & Kirk, J. M. 2004, ApJ, 600, 279
Crutcher, R. M., Wandelt, B., Heiles, C., Falgarone, E., & Troland, T. H. 2010, ApJ, 725, 466
Dobbs, C. L., Burkert, A., & Pringle, J. E. 2011, MNRAS, 413, 2935
Dowell, C. D., Cook, B. T., Harper, D. A., et al. 2010, Proc. SPIE, 7735, 6
Duarte-Cabral, A., & Dobbs, C. L. 2017, MNRAS, 470, 4261
Evans, N. J. I., Heyer, M., Miville-Deschênes, M.-A., Nguyen-Luong, Q., & Merello, M. 2021, ApJ, 920, 126
Fiege, J. D., & Pudritz, R. E. 2000, MNRAS, 311, 85
Friesen, R. K., Pineda, J. E., co-PIs, et al. 2017, ApJ, 843, 63
Girart, J. M., Rao, R., & Marrone, D. P. 2006, Sci, 313, 812
Goodman, A. A., Alves, J., Beaumont, C. N., et al. 2014, ApJ, 797, 53
Grudić, M. Y., Guszejnov, D., Hopkins, P. F., Offner, S. S. R., & Faucher-Giguère, C.-A. 2021, MNRAS, 506, 2199
Grudić, M. Y., Guszejnov, D., Offner, S. S. R., et al. 2022, MNRAS, 512, 216
Grudić, M. Y., Hopkins, P. F., Lee, E. J., et al. 2019, MNRAS, 488, 1501
Guzmán, A. E., Sanhueza, P., Contreras, Y., et al. 2015, ApJ, 815, 130
Hacar, A., Clark, S. E., Heitsch, F., et al. 2023, in ASP Conf. Ser. 534, Protostars and Planets VII, ed. S. Inutsuka et al. (San Francisco, CA: ASP), 153
Harper, D. A., Runyan, M. C., Dowell, C. D., et al. 2018, JAI, 7, 1840008
Hix, R., He, C.-C., & Ricotti, M. 2023, MNRAS, 522, 6203
Hogge, T., Jackson, J., Stephens, I., et al. 2018, ApJS, 237, 27
Hull, C. L. H., Plambeck, R. L., Bolatto, A. D., et al. 2013, ApJ, 768, 159
Hull, C. L. H., Plambeck, R. L., Kwon, W., et al. 2014, ApJS, 213, 13
Jackson, J. M., Finn, S. C., Chambers, E. T., Rathborne, J. M., & Simon, R. 2010, ApJL, 719, L185
Jackson, J. M., Rathborne, J. M., Foster, J. B., et al. 2013, PASA, 30, 57
Jackson, J. M., Rathborne, J. M., Shah, R. Y., et al. 2006, ApJS, 163, 145
Jadhav, O. R., Dewangan, L. K., Haj Ismail, A., et al. 2025, ApJ, 986, 48
Kauffmann, J., Bertoldi, F., Bourke, T. L., Evans, N. J., II, & Lee, C. W. 2008, A&A, 487, 993
Koch, E. W., & Rosolowsky, E. W. 2015, MNRAS, 452, 3435
Kovács, A. 2008a, Proc. SPIE, 7020, 70201S
Kovács, A. 2008b, Proc. SPIE, 7020, 702007
Lee, D., Berthoud, M., Chen, C.-Y., et al. 2021, ApJ, 918, 39
Lee, K. I., Dunham, M. M., Myers, P. C., et al. 2015, ApJ, 814, 114
Li, J. J., Immer, K., Reid, M. J., et al. 2022, ApJS, 262, 42
Li, P. S., Lopez-Rodriguez, E., Ajeddig, H., et al. 2022, MNRAS, 510, 6085

McKee, C. F., & Ostriker, E. C. 2007, ARA&A, 45, 565

Molinari, S., Swinyard, B., Bally, J., et al. 2010, A&A, 518, L100

Myers, P. C., Heyer, M., Stephens, I. W., et al. 2025, ApJ, 991, 210

Myers, P. C., Stephens, I. W., & Coudé, S. 2024, ApJ, 962, 64

Ngoc, N. B., Diep, P. N., Hoang, T., et al. 2023, ApJ, 953, 66

Ostriker, E. C., Stone, J. M., & Gammie, C. F. 2001, ApJ, 546, 980

Pattle, K., Fissel, L., Tahani, M., Liu, T., & Ntormousi, E. 2023*(ASP Conf. Ser. 534, Protostars and Planets VII)* ed. S. Inutsuka et al. (San Francisco, CA: ASP), 193

Pattle, K., Ward-Thompson, D., Berry, D., et al. 2017, ApJ, 846, 122

Perault, M., Omont, A., Simon, G., et al. 1996, A&A, 315, L165

Planck Collaboration, Ade, P. A. R., Aghanim, N., et al. 2016, A&A, 586, A138

Price, S. D., Egan, M. P., Carey, S. J., Mizuno, D. R., & Kuchar, T. A. 2001, AJ, 121, 2819

Rao, R., Girart, J. M., Marrone, D. P., Lai, S.-P., & Schnee, S. 2009, ApJ, 707, 921

Reid, M. J., Menten, K. M., Brunthaler, A., et al. 2019, ApJ, 885, 131

Robitaille, T., & Bressert, E., 2012 APLpy: Astronomical Plotting Library in Python, Astrophysics Source Code Library, ascl:1208.017

Robitaille, T., Deil, C., & Ginsburg, A., 2020 reproject: Python-based Astronomical Image Reprojection, Astrophysics Source Code Library, ascl:2011.023

Schuller, F., Urquhart, J. S., Csengeri, T., et al. 2021, MNRAS, 500, 3064

Simon, R., Jackson, J. M., Rathborne, J. M., & Chambers, E. T. 2006, ApJ, 639, 227

Skalidis, R., & Tassis, K. 2021, A&A, 647, A186

Soler, J. D., & Hennebelle, P. 2017, A&A, 607, A2

Soler, J. D., Hennebelle, P., Martin, P. G., et al. 2013, ApJ, 774, 128

Stephens, I. W., Dunham, M. M., Myers, P. C., et al. 2017, ApJ, 846, 16

Stephens, I. W., Looney, L. W., Dowell, C. D., Vaillancourt, J. E., & Tassis, K. 2011, ApJ, 728, 99

Stephens, I. W., Looney, L. W., Kwon, W., et al. 2013, ApJL, 769, L15

Stephens, I. W., Myers, P. C., Zucker, C., et al. 2022, ApJL, 926, L6

Vaillancourt, J. E. 2006, PASP, 118, 1340

van Hoof, P. A. M. 2000, MNRAS, 314, 99

Wu, Y. W., Sato, M., Reid, M. J., et al. 2014, A&A, 566, A17

Zhang, M., Kainulainen, J., Mattern, M., Fang, M., & Henning, T. 2019, A&A, 622, A52

Zhao, B., Pudritz, R. E., Pillsworth, R., Robinson, H., & Wadsley, J. 2024, ApJ, 974, 240

Zucker, C., Battersby, C., & Goodman, A. 2015, ApJ, 815, 23

Zucker, C., Battersby, C., & Goodman, A. 2018, ApJ, 864, 153

Zucker, C., & Chen, H. H.-H. 2018, ApJ, 864, 152

Zucker, C., Smith, R., & Goodman, A. 2019, ApJ, 887, 186